Limb–nadir matching using non-coincident NO2 observations: Proof of concept and the OMI-minus-OSIRIS prototype product

Cristen Adams[1,2], Elise N. Normand[1], Chris A. McLinden[3], Adam E. Bourassa[1], Nicholas D. Lloyd[1], Douglas A. Degenstein[1], Nickolay A. Krotkov[4], Maria Belmonte Rivas[5], K. Folkert Boersma[5,6], Henk Eskes[5]

[1] Institute of Space and Atmospheric Studies, University of Saskatchewan, Saskatoon, Canada

[2] Alberta Environmental Monitoring, Evaluation, and Reporting Agency, Edmonton, Canada

[3] Air Quality Research Division, Environment Canada, Toronto, Ontario

[4] NASA Goddard Space Flight Center, Greenbelt, MD, USA

[5] Royal Netherlands Meteorological Institute (KNMI), De Bilt, The Netherlands

[6] Wageningen University, Meteorology and Air Quality Group, Wageningen, The Netherlands

Correspondence to: Cristen Adams (cristenlfadams@gmail.com)

Abstract

A variant of the limb-nadir matching technique for deriving tropospheric NO_2 columns is presented in which the stratospheric component of the NO_2 slant column density (SCD) measured by the Ozone Monitoring Instrument (OMI) is removed using non-coincident profiles from the Optical Spectrograph and InfraRed Imaging System (OSIRIS). In order to correct their mismatch in local time and the diurnal variation of stratospheric NO_2, OSIRIS profiles, which were measured just after sunrise, were mapped to the local time of OMI observations using a photochemical box model. Following the profile time adjustment, OSIRIS NO_2 stratospheric vertical columns densities (VCDs) were calculated. For profiles that did not reach down to the tropopause, VCDs were adjusted using the photochemical model. Using air mass factors from the OMI Standard Product (SP), a new tropospheric NO_2 VCD product – referred to as OMI-

Atmospheric
Measurement
Techniques
Open Access
Discussions
EGU

1   minus-OSIRIS (OmO) – was generated through limb-nadir matching. To accomplish this, the

2   OMI total SCDs were scaled using correction factors derived from the next-generation SCDs

3   that improve upon the spectral fitting used for the current operational products. One year, 2008,

4   of OmO was generated for 60°S to 60°N and a cursory evaluation was performed. The OmO

5   product was found to capture the main features of tropospheric NO_2 including a background

6   value of about 0.3×10^{15} molecules/cm^2 over the tropical Pacific and values comparable to the

7   OMI operational products over anthropogenic source areas. While additional study is required,

8   these results suggest that a limb-nadir matching approach is feasible for the removal of

9   stratospheric NO_2 measured by a polar orbiter from a nadir-viewing instrument in a

10   geostationary orbit such as Tropospheric Emissions: Monitoring of Pollution (TEMPO) or

11   Sentinel-4.

12

13   **1   Introduction**

14   Nadir satellite instruments can measure daily global maps of tropospheric nitrogen dioxide

15   (NO_2), which, at the surface, is a pollutant linked to smog and acid rain. Tropospheric NO_2 was

16   first successfully retrieved from the Global Ozone Monitoring Experiment (GOME) (Burrows

17   et al., 1999), and has since also been measured by the Scanning Imaging Absorption

18   Spectrometer for Atmospheric Chartography (SCIAMACHY) (Bovensmann et al., 1999),

19   Ozone Monitoring Instrument (OMI) (Levelt et al., 2006) and GOME 2 (Callies et al., 2000)

20   nadir-viewing instruments.

21   High concentrations of NO_2 are also found in the stratosphere, where NO_2 has a large seasonal

22   and diurnal variability due to photochemistry, and, in some case, due to dynamics as well (e.g.,

23   Dirksen et al., 2011). Therefore retrievals for tropospheric NO_2 from nadir instruments

24   typically rely on extrapolation or assimilation approaches to determine the stratospheric

25   contribution to NO_2. A correct and unbiased removal of stratospheric NO_2 is a major challenge

26   and represents a significant source of uncertainty in tropospheric NO_2 retrieval products.

27   Various methods have been used to separate stratospheric and tropospheric contributions from

28   the total NO_2 vertical column density (VCD) measured by nadir satellites. Several of these

29   techniques assume that the NO_2 distribution over a remote, non-polluted location, like the

30   Pacific Ocean, is dominated by the stratospheric component. These stratospheric NO_2 values

31   are then extrapolated to other locations. Hilboll et al. (2013) give a good overview of the

32   development of these methods from early analyses, which assumed that stratospheric NO_2 does

1   not vary within a latitude band (Martin et al., 2002; Richter and Burrows, 2002) to more

2   complex techniques, such as the planetary wave-2 zonal analysis technique (Bucsela et al.,

3   2006). Chemical transport model information can also be used to infer stratospheric NO_2.. In

4   order to account for biases between the modeled stratosphere and the satellite measurements,

5   the model data can be scaled to the satellite measurements through comparisons in the Pacific

6   Ocean (Richter et al., 2005) or the measured total column NO_2 can be assimilated in the model

7   (e.g., Boersma et al., 2007). These techniques, as applied to operational data products for OMI,

8   are described in more detail in Sect. 2.1. Another approach is the cloud slicing method

9   (Belmonte Rivas et al., 2015; Choi et al., 2014), which yields information on the NO_2 vertical

10   profile. When there is cloud cover, the lower part of the atmosphere is obscured, so the levels

11   of NO_2 in various layers of the atmosphere above the clouds can be inferred. This approach is

12   not currently used for any operational data products.

13   Another promising technique involves using the global, vertically resolved stratospheric NO_2

14   profiles from satellite instruments that measure in the limb-viewing geometry. Near-daily

15   global resolution can be obtained using limb instruments that measure scattered sunlight, such

16   as the Optical Spectrograph and InfraRed Imaging System (OSIRIS) (Llewellyn et al., 2004;

17   McLinden et al., 2012b) and SCIAMACHY (Bovensmann et al., 1999), as well as instruments

18   that measure emissions, such as the Michelson Interferometer for Passive Atmospheric

19   Sounding (MIPAS) (Fischer et al., 2008) and the High Resolution Dynamics Limb Sounder

20   (HIRDLS) (Gille et al., 2008). These limb-viewing measurements of stratospheric NO_2 can

21   then be matched to and subtracted from the nadir total column measurement.

22   The limb-nadir matching method has been employed for SCIAMACHY NO_2 (Beirle et al.,

23   2010; Hilboll et al., 2013; Sierk et al., 2006; Sioris et al., 2004), which provides both limb and

24   nadir measurements virtually simultaneously and at the same local time. In the most recent

25   analysis, Hilboll et al. (2013) calculate a stratospheric NO_2 VCD from limb measurements for

26   each nadir measurement. They adjust the stratospheric VCDs to match the levels observed in

27   the nadir columns using a latitude-dependent factor calculated daily over the Pacific Ocean,

28   where levels of tropospheric NO_2 are expected to be low. Since the SCIAMACHY limb and

29   nadir instruments measure at the same local time, the diurnal variation of NO_2 does not

30   complicate the limb-nadir matching.

31   In this proof of concept study, the potential of deriving tropospheric NO_2 from measurements

32   taken by limb and nadir instruments at different local times is explored. OSIRIS limb-viewing

1   stratospheric NO_2 from the descending node of the orbit, measured toward sunrise, and OMI

2   nadir-viewing column NO_2, measured near midday, are used to quantify the abundance of

3   tropospheric NO_2.   OMI tropospheric NO_2 has been well-characterized against other

4   instruments (Boersma et al., 2011; Lamsal et al., 2014) and has been used in many scientific

5   studies of tropospheric air pollution (e.g., Duncan et al., 2016; Krotkov et al., 2016; McLinden

6   et al., 2012a; Russell et al., 2012; Veefkind et al., 2011; Zhou et al., 2012) as well as some work

7   on stratospheric NO_2 (e.g., Dirksen et al., 2011). OSIRIS stratospheric NO_2 agrees well with

8   other instruments (Brohede et al., 2007; Kerzenmacher et al., 2008) and provides daily near-

9   global coverage, which is necessary to match to OMI measurement dates and locations. The

10   resulting tropospheric VCDs are referred to as the OMI–minus–OSIRIS (OmO) data product.

11   Although, the local time mismatch between OSIRIS and OMI adds a significant complication

12   due to the diurnal nature of NO_2, it is also a more realistic scenario in the merging of limb

13   measurements for some future missions. Nadir-viewing instruments on geostationary platforms

14   such as the Tropospheric Emissions: Monitoring of Pollution (TEMPO) (Chance et al., 2013;

15   Zoogman et al., 2014), Sentinel-4 (Ingmann et al., 2012), and Geostationary Environmental

16   Monitoring Spectrometer (GEMS) (Kim, 2012) will be measuring throughout the sunlit day at

17   many local times. These measurements could be paired with limb-viewing instruments on polar

18   orbiters. Ideally, a limb-nadir merging would be carried out through a data assimilation system,

19   but it is important nonetheless to understand their compatibility in a much simpler framework.

20   In order to create the OmO dataset, the following steps were taken. OSIRIS, OMI, and

21   photochemical model data were used, as described in Sect. 2. A series of 3-day average

22   stratospheric VCD maps on a uniform latitude and longitude grid were created from OSIRIS

23   data for various local times, using scale factors from the photochemical model, as described in

24   Sect. 3. The OmO data product was then calculated using OMI VCDs and air mass factors

25   (AMFs), along with matched stratospheric VCDs interpolated from the OSIRIS VCD maps.

26   These calculations and a correction factor for a known bias in the OMI data (Marchenko et al.,

27   2015; van Geffen et al., 2015), as well as an assessment of the OmO prototype data, are

28   described in Sect. 4. A discussion of these results and future applications is given Sect. 5.

29

Atmospheric
Measurement
Techniques

Open Access

Discussions

EGU

2 Measurements and Modelling Tools

2.1 OMI on Aura

OMI (Levelt et al., 2006) is a nadir-viewing solar backscatter spectrometer on-board the Aura satellite (Schoeberl et al., 2006), which was launched into a polar orbit about the Earth on 15 July 2004. The satellite was designed to further our understanding of stratospheric and tropospheric chemistry as well as climate systems through high spectral resolution measurements in the UV/visible (270–500 nm). OMI follows a sun-synchronous orbit with a 98.2° inclination and an ascending equatorial node crossing of approximately 13:45 local time. OMI captures a 114° field of view, which covers a width of 2600 km. The swath direction is perpendicular to the satellite flight path, so with 14 orbits per day there is near complete global coverage. There are a total of 60 binned pixel positions across the entire swath with an outermost swath-angle of 57°. In the centered nadir position, the ground pixel size covers 13×24 km^2 (along track by across track) for the UV-2 and visible channels, and 13×48 km^2 for the UV-1 channel. As the swath-angle increases, the pixel footprint increases to a maximum of $\sim 15 \times 150$ km^2 at the outermost pixel positions. NO_2 is retrieved with the visible channel between 405 and 465 nm, where there is little interference from other absorbers.

There are two operational NO_2 data products: the Dutch-OMI NO_2 (DOMINO v2) product (Boersma et al., 2011) and the NASA standard product (SP v2) (Bucsela et al., 2013). These two data products are referred to as OMI-SP and OMI-DOMINO, respectively, throughout this paper. Both products employ a multi-step approach with a common first step. Differential optical absorption spectroscopy (DOAS) is used to determine the NO_2 slant column densities (SCDs) by fitting the ratio of earthshine radiance to extra-terrestrial irradiance spectra to laboratory reference data, Ring spectrum (Chance and Spurr, 1997) and polynomial. Physically, the SCD represents the total absorption by NO_2 along the average path of the sunlight through the atmosphere, which includes absorption in both the stratosphere and troposphere.

Different approaches are used for the second step, which is to execute the stratosphere-troposphere separation. OMI-DOMINO accomplishes stratosphere-troposphere separation by assimilating the OMI slant columns within the TM4 chemistry-transport model (Boersma et al., 2007; Dirksen et al., 2011), effectively determining how much NO_2 resides in the stratosphere, which is then subtracted from the total slant column. For OMI-SP, the stratospheric column is

Atmospheric
Measurement
Techniques
Discussions

1   recovered by performing a local analysis of the stratospheric field in cloudy regions or regions

2   where there is no tropospheric pollution. These values are then extrapolated to polluted regions

3   using spatial interpolation and smoothing technique technique (Bucsela et al., 2013), which

4   assumes that changes in tropospheric NO_2 occur on relatively shorter geographical scales than

5   stratospheric ones.

6   The final step for both operational NO_2 data products is the determination of the tropospheric

7   VCD from the residual SCD in the troposphere. In general, the total SCD, S, is related to the

8   total VCD, V, through the tropospheric air mass factor (AMF), A, by, $S = V \cdot A$ and is a

9   measure of the changes in absorption when light traverses an effective or "slant" path through

10 a tropospheric layer. The AMF is dependent on the path length, which in turn depends on the

11 solar zenith angle (SZA), the satellite viewing angle, the vertical distribution of absorbing

12 species, cloud and aerosol properties, and albedo. In the troposphere, a key dependence is the

13 vertical distribution of NO_2 which is taken from model simulations: the TM4 model (at the time

14 of the measurement) for the DOMINO product and the Global Modeling Initiative (GMI) model

15 (monthly) for the SP product. AMFs are calculated using radiative transfer models that

16 accurately simulate absorption, multiple-scattering, and surface reflection.

17 The OmO prototype dataset was constructed using the AMFs and VCDs from the OMI-SP v2

18 dataset (Bucsela et al., 2013). An alternate OmO-DOMINO prototype was also constructed

19 using OMI-DOMINO v2.0 (Boersma et al., 2011) AMFs and VCDs. The OSIRIS stratospheric

20 VCDs and OmO tropospheric VCDs were compared with both OMI-SP and OMI-DOMINO

21 v2.0. For all figures and statistics presented in this paper, OMI and OmO data for OMI cloud

22 radiance fractions (CRF) < 0.3 and SZA < 75 ° were used. Additionally, OMI pixels affected

23 by the row anomaly were removed. Note that both the OMI-SP and OMI-DOMINO retrieval

24 algorithms correct for across-track variability, or stripes, for pixels that are not affected by the

25 row anomaly.

26 **2.2 OSIRIS on Odin**

27 OSIRIS (Llewellyn et al., 2004; McLinden et al., 2012b) measures the atmospheric limb

28 radiance of scattered sunlight as a function of tangent altitude from the upper troposphere to the

29 lower mesosphere. This Canadian instrument is on-board Odin (Murtagh et al., 2002), a

30 Swedish satellite, which was launched 20 February 2001 into a sun-synchronous orbit near 600

31 km in altitude with about a 90-minute period. The satellite track is near-terminator and closely

1 follows the local dusk and dawn terminators on the ascending and descending tracks with

2 northward and southward equatorial crossings at 18:00 and 06:00 local time, respectively.

3 OSIRIS has near-global coverage from 82°S to 82°N with an orbital inclination of 98° from the

4 equator. At the tangent point, the atmosphere is in darkness when the SZA is greater than 90°;

5 the winter hemisphere is largely darkened at the local time of the measurements.

6 OSIRIS includes an optical spectrograph, which is comprised of an optical grating and a charge-

7 coupled device detector, and an infrared imager. Atmospheric limb radiance is measured by the

8 optical spectrograph between 280 and 810 nm with a spectral resolution of about 1 nm. Vertical

9 profiles from approximately 7 to 110 km in tangent altitude are acquired by nodding the

10 spacecraft. The field of view at the tangent point is roughly 40×1 km^2 (horizontal by vertical)

11 and successive measurements are separated by about 2 km tangent altitude.

12 In this work, stratospheric profiles from the v5.0 NO$_2$ dataset (Haley and Brohede, 2007) were

13 used. Slant column densities are retrieved in the 435-451 nm range, using the DOAS technique.

14 NO$_2$ profiles are then retrieved using an optimal estimation technique on a fixed retrieval grid,

15 from 10-46 km at 2 km intervals. The OSIRIS NO$_2$ stratospheric VCDs agree to within

16 0.25×10^{15} molecules/cm^2 of the other limb instruments for most latitudes and seasons, as shown

17 in Appendix A.

18 OSIRIS data from the descending node only were used in this analysis. Due to the diurnal

19 variation of NO$_2$, there are systematic differences between descending and ascending track

20 measurements, which are taken at morning and evening local times respectively. The

21 descending node was selected because in the ascending node OSIRIS measures at larger SZAs,

22 leading to fewer valid measurements in the winter hemisphere. Furthermore, the solar

23 scattering angle on the ascending track is closer to the forward scattering scenario, which causes

24 clouds and aerosols to appear very bright leading to the saturation of pixels and the rejection of

25 some measurements.

26 Additionally, only data for SZA < 88° were used. This largely eliminates errors introduced by

27 the "diurnal effect", also called "chemical enhancement" (Hendrick et al., 2006; McLinden et

28 al., 2006), which is not currently accounted for in the NO$_2$ retrieval. This occurs because

29 sunlight passes through a range of SZAs in the atmosphere before reaching the OSIRIS

30 instrument, and therefore samples NO$_2$ at different points in its diurnal cycle. This effect is

31 largest toward SZA = 90°, where NO$_2$ varies rapidly.

1   The 2008 period was chosen because it covers the time when the descending node measurement

2   time drifts closest to 07:00 before the sampling time drifts back toward 06:00. This maximizes

3   the number of valid descending node measurements.

4   **2.3   Photochemical box model**

5   In this work, a stratospheric photochemical box model (Brohede et al., 2008; McLinden et al.,

6   2000; Prather, 1992), is employed to simulate the NO_2 diurnal cycle (see Sect. 3.1) and to adjust

7   OSIRIS stratospheric VCDs for NO_2 profiles that terminate above the tropopause (see Sect.

8   3.2).   For a particular simulation, the background pressure and temperature atmospheric

9   profiles, ozone, long-lived tracers (N_2O, H_2O, CH_4), and the NO_y, Cl_y, and Br_y families need to

10   be specified for each altitude of the OSIRIS profiles. All remaining species are calculated to be

11   in a 24-h steady-state by integrating the model over 30 days, but fixed to a given Julian day.

12   Heterogeneous chemistry on background stratospheric aerosols is prescribed by the model, but

13   no polar stratospheric clouds are included.

14   For the present study, the photochemical model was run at each altitude layer of every OSIRIS

15   NO_2 profile measurement. N_2O, CH_4, NO_y, Cl_y, and Br_y from the Canadian Middle Atmosphere

16   Model (CMAM) (Jonsson et al., 2004; Scinocca et al., 2008) were interpolated to the month

17   and latitude of the OSIRIS NO_2 measurement. H_2O was derived from tracer correlations with

18   CH_4 (McLinden et al., 2000). OSIRIS ozone profiles (Degenstein et al., 2009), measured at the

19   same time as NO_2, were included in the analysis. Outside of the OSIRIS ozone altitude range

20   and for scans with missing ozone data, the CMAM ozone climatology (Jonsson et al., 2004;

21   Scinocca et al., 2008) was used. Albedo was also from OSIRIS retrievals (Degenstein et al.,

22   2009) from the same scan as the NO_2 measurement. Aerosol extinction was interpolated from

23   2-week OSIRIS aerosol extinction averages (Rieger et al., 2015) and converted to aerosol

24   surface area assuming a lognormal distribution with a mode radius of 80 nm and a mode width

25   of 1.6, which is consistent with the OSIRIS aerosol retrieval assumptions. Pressure and

26   temperature profiles were obtained from the European Centre for Medium-Range Weather

27   Forecasts (ECWMF) analysis data for the time and location of each OSIRIS scan.

28

29   **3   OSIRIS Stratospheric VCD Maps**

30   In order to create the OmO data product, stratospheric VCDs must be available at the latitude,

31   longitude, date, and local time of each OMI measurement. Therefore, individual OSIRIS

Atmospheric
Measurement
Techniques
Discussions

1   stratospheric profiles were scaled to a uniform grid of local times using the photochemical box

2   model and stratospheric VCDs were calculated from these profiles. The stratospheric VCDs

3   were gridded uniformly in space and time, so that they could be interpolated to OMI

4   measurements latitude, longitude, date, and local time. The detailed procedure used to create

5   the OSIRIS stratospheric VCD maps is described in this section.

6   ## 3.1   Scaling the local time of OSIRIS measurements

7   A key challenge in comparing and merging measurements of stratospheric NO_2 made at

8   different local times lies in reconciling the impact of its diurnal cycle due to photochemistry.

9   For a detailed description of the diurnal variation of NO_2 and its impact on comparisons

10   between satellite instruments, see, e.g., Belmonte Rivas et al. (2014). Over short time-scales

11   (~1 minute), NO_2 and NO are in fast photochemical equilibrium and are referred to as NO_x.

12   Since NO is produced by the photolysis of NO_2, more NO_x is in the form of NO_2 when there is

13   less available sunlight. Therefore, levels of NO_2 are typically lower during the day than

14   overnight, with sharp gradients over sunrise and sunset. Furthermore, slower reactions affect

15   the overall amount of NO_x available. The most significant of these reactions is the reaction

16   with N_2O_5, which occurs over longer time-scales (~hours to days): overnight NO_x is converted

17   to N_2O_5 and during the day it is released again, causing the amount of NO_2 at sunset to be higher

18   than the amount of NO_2 at sunrise.

19   The local times of OSIRIS and OMI measurements are shown in Figure 1. At most latitudes,

20   OSIRIS measurements are taken at local times in the morning, while OMI measurements are

21   taken in the early afternoon. This affects the matching of OSIRIS and OMI datasets for the

22   calculation of the OmO data product. For example, at low latitudes, OSIRIS descending node

23   measurements are taken shortly after sunrise, when due to the photochemistry described above,

24   there is less NO_2 in the stratosphere than during the OMI afternoon measurements. Therefore,

25   the diurnal variation of NO_2 must be accounted for before subtracting OSIRIS stratospheric

26   NO_2 from the OMI measurements.

27   The photochemical box model (see Sect. 2.3) was used to adjust, or map, the local time by

28   applying a photochemical scaling factor to each layer in the profile (z). This is shown in Eq.

29   (1):

30   $$\rho_{OSIRIS}(z, t_{new}) = \rho_{OSIRIS}(z, t_{OSIRIS}) \cdot \frac{\rho_{model}(z, t_{new})}{\rho_{model}(z, t_{OSIRIS})} \quad , \qquad (1)$$

Atmospheric
Measurement
Techniques
Discussions

1   where ρ_{OSIRIS} and ρ_{model} are the OSIRIS and modelled NO_2 number densities at a given altitude

2   layer, respectively, and t_{OSIRIS} and t_{new} are the local times of the OSIRIS measurement and the

3   new adjusted time. This approach has been successfully applied using the same photochemical

4   box model to the validation of NO_2 profiles (Brohede et al., 2007) and the merging of data

5   products (Brohede et al., 2008).

6   **3.2   OSIRIS stratospheric VCD calculations**

7   Stratospheric NO_2 VCDs were calculated from OSIRIS profiles that had been adjusted to the

8   desired local time. When NO_2 profile data is available from the tropopause (z_{trop}) to the top of

9   the atmosphere (z_{toa}), the stratospheric VCD is the integral of the NO_2 number densities over

10   altitude layers, as shown in Eq. (2).

11   $$V_{strat} = \int_{z_{trop}}^{z_{toa}} \rho(z)dz \qquad . \qquad (2)$$

12   OSIRIS v5.0 NO_2 profiles extend to 46 km, which is effectively the top of atmosphere since

13   NO_2 number densities are very low above this altitude. The altitude of the thermal tropopause

14   was calculated using lapse rates from the National Center for Environmental Prediction (NCEP)

15   reanalysis data (Kalnay et al., 1996). The OMI-DOMINO algorithm also uses the thermal

16   tropopause (Dirksen et al., 2011), but the OMI-SP algorithm uses a dynamical tropopause

17   definition (Bucsela et al., 2013). The method used to calculate the tropopause is expected to

18   have a minimal impact on stratospheric VCDs because concentrations of NO_2 are small near

19   the tropopause. Furthermore, the tropopause definition was found to have very little effect on

20   the OMI-SP retrievals (Bucsela et al., 2013).

21   For OSIRIS profiles that extend to or below the thermal tropopause, the NO_2 number density

22   was interpolated to the tropopause altitude and a trapezoidal integration was performed from

23   the tropopause to the top of the NO_2 profile to calculate the stratospheric VCD. For OSIRIS

24   profiles that do not extend below the tropopause, the stratospheric VCD was calculated using

25   information from the photochemical model, as shown in Eq. (3):

26   $$V_{strat} = V_{part}^{OSIRIS} \cdot \left(V_{strat}^{model} \middle/ V_{part}^{model} \right) . \quad (3)$$

27   The modelled stratospheric VCD (V_{strat}^{model}) was integrated using the same technique as for

28   the OSIRIS profiles that extend below the tropopause (Eq. (2)). Partial VCDs from the OSIRIS

Atmospheric
Measurement
Techniques
Open Access
Discussions
EGU

1   ($V_{part}{}^{OSIRIS}$) and model profiles ($V_{part}{}^{model}$) were calculated by a summation over the altitude

2   layers with valid OSIRIS NO_2 measurements, as shown in Eq. (4):

3    $$V_{part} = \sum_{z\_min}^{z\_max} \rho(z_i) \cdot \Delta z \quad , (4)$$

4   where z_min and z_max are the minimum and maximum altitude levels of available NO_2 data

5   in the given OSIRIS profile and Δz is the altitude difference between OSIRIS profile layers,

6   which is 2-km for the OSIRIS v5.0 NO_2 dataset. This summation technique was chosen for the

7   calculation of the partial stratospheric columns because, compared with a trapezoidal

8   integration, this maximized the amount of information coming from the lowermost available

9   layer of the OSIRIS measurements.

10   Figure 2 shows statistics for the lowest altitude of the OSIRIS measurement relative to the

11   thermal tropopause for individual scans. Negative altitude differences indicate that OSIRIS

12   measured to altitudes below the thermal tropopause. Positive altitude differences indicate that

13   the OSIRIS profiles terminated above the thermal tropopause and that therefore the OSIRIS

14   VCDs were scaled to the full atmosphere using Eq. (3). For 45°S to 45°N, median altitude

15   differences are negative, indicating the more than 50% of the profiles reach the tropopause.

16   Between 65°S and 55°N, 75% of the profiles reach within 4 km of the tropopause. At high

17   latitudes, the tropopause can be very low and therefore more OSIRIS profiles terminate higher

18   above the tropopause. In order to avoid relying too heavily on the model scale factors at high

19   latitudes, the OmO data product was calculated between 60°S and 60°N only. Additionally,

20   profiles that terminate > 5 km above the tropopause were excluded from the analysis.

21   OSIRIS profiles that extended below the tropopause were used to test the effect of the VCD

22   scaling given in Eq. (3). The results of these tests are shown in Figure 3. VCD_{strat}^{full} are the

23   OSIRIS stratospheric VCDs calculated using the full OSIRIS profiles and Eq. (2). Data from

24   the same OSIRIS profiles are removed for two layers above the tropopause. This yields profiles

25   that, on average, terminate 3.4 km above the tropopause. VCD_{strat}^{cor} is then calculated from these

26   profiles using Eq. (3). At most latitudes, VCD_{strat}^{cor} is within 2% of VCD_{strat}^{full}, which amounts

27   to roughly 5×10^{13} molecules/cm^2 of the stratospheric VCD, suggesting that the model

28   corrections are performing well. This yields conservative estimates because most OSIRIS

29   profiles used in this analysis extend closer to the tropopause, as shown in Figure 2. However,

30   it should be noted that there is a sampling bias in these tests as OSIRIS profiles that extend

31   below the tropopause are more often available for higher tropopauses.

Atmospheric
Measurement
Techniques
Discussions

Open Access

3.3   Calculation of gridded stratospheric VCD maps

For interpolation to OMI measurements (latitude, longitude, date, local time), daily sets of OSIRIS VCD maps were created for hourly local times, ranging from 0-23 hours. Note that the hourly local time resolution of these maps is sufficient for interpolation to OMI NO_2 measurements because OMI measures for SZA $< 80°$ when NO_2 is not varying rapidly with local time.

In order to calculate these maps, OSIRIS profiles for the time-period of interest were selected. Profiles for 65°S to 65°N were used to produce VCD maps that were reliable for 60°S to 60°N, the latitude range over which OmO is calculated. These profiles were scaled to the 0-23 hour local time grid using the photochemical box model (see Sect. 3.1) and stratospheric VCDs were calculated from these profiles (see Sect. 3.2). For each local time, a filtering function was applied to the stratospheric VCDs in order to ensure a smooth field and account for irregular sampling. The filtering algorithm calculates the great circle distances between the regular grid-point and each sparse VCD data point in latitude and longitude. It then averages the sparse data at the grid-point, weighting it by a Gaussian function of the great circle distances in latitude and longitude. If the total weight of data at a given grid-point is < 1, the grid-point is left empty. This essentially smooths the data to a finer grid; a 1° latitude and 1° longitude grid was used here.

Various combinations of Gaussian weighting standard deviations and time averaging windows (1-day, 2-day, 3-day, and 5-day) were tested. A three day averaging window was selected, i.e., each daily map includes measurements from the given date, the previous day, and the next day. Standard deviations for the Gaussian weighting of 6° in latitude and 10° longitude were chosen, reflecting the spatial coverage of OSIRIS measurements. These settings yield good spatial coverage in the stratospheric maps, while providing reasonable resolution of features in the VCDs. Due to the averaging and smoothing of the data, rapid changes or sharp spatial gradients in NO_2, for example when vortex remnants reach mid-latitudes, may be smoothed out. This is a limitation of OSIRIS sampling.

Figure 4 shows examples of the OSIRIS VCD maps for 4 March 2008 and 21 June 2008 at the approximate OSIRIS and OMI measurement times. Note that, as described above, each of these maps is made up using 3 days of OSIRIS data. The 4 March VCD maps have global coverage from 65°S to 65°N, the latitude range over which OSIRIS profiles were included in the analysis. The 21 June maps have limited coverage in the southern hemisphere. This is because OSIRIS

1   does not measure NO_2 in the winter hemisphere. The VCD maps for 07:00 LT, the approximate

2   OSIRIS measurement time, have lower levels of NO_2 than the VCD maps for 13:00 LT, the

3   approximate OMI measurement time. These differences with local time are typically ~0.4-

4   0.5×10^{15} molecules/cm^2, and can locally reach values of up to ~1×10^{15} molecules/cm^2. This

5   demonstrates the effect of the diurnal scaling of NO_2 prior to matching the OSIRIS and OMI

6   measurements.

7

8   **4   Calculation of OMI-minus-OSIRIS (OmO) Tropospheric NO_2**

9   This section describes the steps involved in creating the OmO prototype dataset, using

10   stratospheric VCDs from OSIRIS and AMFs and VCDs from the operational OMI-SP data

11   product, and presents comparisons of the OmO and OMI operational datasets. OSIRIS

12   stratospheric VCD maps were interpolated to the OMI measurement date, location and local

13   time. The interpolated OSIRIS stratospheric VCDs were compared against OMI-SP and OMI-

14   DOMINO stratospheric VCDs, as described in Sect. 4.1. Corrections for a known high bias in

15   OMI SCDs are presented in Sect. 4.2. OmO tropospheric NO_2 VCDs were calculated using to

16   the equations given in Sect. 4.3. The quality of the matching between the OMI and OSIRIS

17   stratospheres is discussed in Sect. 4.4, and the OmO tropospheric VCDs are presented and

18   assessed in Sect. 4.5. In Sect. 4.6, an alternate OmO-DOMINO tropospheric VCD dataset is

19   constructed and is used to interpret the relative contributions of the data used to calculate OmO.

20   **4.1   Comparison of Stratospheric VCDs from OMI-SP and OSIRIS**

21   In order to obtain an OSIRIS stratospheric VCD for each OMI pixel, a linear interpolation in

22   latitude, longitude, and local time was performed over the OSIRIS stratospheric VCD maps

23   (see Sect. 3.3) corresponding to the OMI measurement day. Figure 5 shows the number of

24   OMI-SP measurements that were successfully matched to the OSIRIS stratosphere using the

25   OSIRIS gridded VCD maps. In the tropics ~90% of OMI profiles were matched to the OSIRIS

26   stratosphere. Toward mid-latitudes, this drops to ~75-80% in the northern hemisphere and ~60-

27   70% in the southern hemisphere, because OSIRIS coverage is limited to the summer

28   hemisphere.

29   Figure 6 shows a comparison between OMI-SP stratospheric VCDs and OSIRIS stratospheric

30   VCDs, interpolated from the VCD maps. Percent differences in VCD were binned according

31   to latitude and month for 2008. The OSIRIS VCDs are smaller than the OMI-SP VCDs for all

Atmospheric
Measurement
Techniques
Discussions

1   latitudes and months, with percent differences of ~ -20% to -30% in the tropics and ~ -15% to

2   -25% at mid-latitudes. This is due to a known bias in the OMI data, as discussed in Sect. 4.2.

3   For the most-part, percent differences at a given latitude are reasonably consistent across

4   months. This suggests that the modelled diurnal variation scale factors, which vary seasonally,

5   are performing well. There are, however, some outliers, particularly in the winter hemisphere

6   for April – July for 15°S to 35°S and November – December for 25°N to 45°N. The largest

7   discrepancies occur toward the edge of the OSIRIS measurement range, and are therefore may

8   suggest uncertainties in the OSIRIS measurements and/or photochemical model scale factors

9   for larger SZAs ~85-88° at these latitudes.

10

11   **4.2   OMI SCD Bias Correction**

12   A high bias in the OMI stratospheric VCDs has been observed in comparisons with other

13   satellite instruments (Belmonte Rivas et al., 2014) and is largely explained by a known high

14   bias in the OMNO2A v1 SCDs of roughly 20-30% due to issues with the spectral fitting

15   (Marchenko et al., 2015; van Geffen et al., 2015). The OMNO2A v1 SCDs are used for both

16   the OMI-DOMINO v2.0 and OMI-SP v2.1 retrievals. OMI tropospheric VCDs are ~10-15%

17   smaller in polluted regions and ~30% smaller in non-polluted regions after SCDs are corrected

18   for the spectral fitting bias (Marchenko et al., 2015).

19   In order to match the OSIRIS stratospheric VCDs to the OMI measurements, the OMI total

20   SCD must be corrected for its high bias. Marchenko et al. (2015) found that the best predictor

21   of the relative SCD bias is the SCD itself, with small SCDs ($<5\times10^{15}$ molecules/cm^2) having a

22   ~30% positive bias and large SCDs ($\sim5\times10^{16}$ molecules/cm^2) a ~10% bias. Therefore, the

23   SCD-dependent correction factors shown in Table 1 were applied to the OMI total SCDs, using

24   the methodology described in Sect. 3.3. Outside the range of SCDs listed in Table 1, correction

25   factors were estimated using a linear extrapolation.

26   Figure 7 shows an example of bias correction factors, for all OMI-SP measurements on 4 March

27   2008. The correction factors vary with latitude, with values closer to one at higher latitudes,

28   where SCDs are larger. The shape of this curve is consistent with the variation in biases

29   between the OSIRIS and OMI-SP stratospheric VCD datasets, as shown in Sect. 4.1. At

30   northern hemisphere mid-latitudes, there is a wider range of bias correction factors because a

31   larger range of SCDs are observed in polluted regions.

1   **4.3   Calculation of OMI-minus-OSIRIS Tropospheric VCD**

2   This section outlines the methodology used to calculate the OmO tropospheric NO_2 VCD data

3   product. The OMI total SCD (S_{tot}^{OMI}) can be expressed as the sum of the stratospheric and

4   tropospheric SCDs (S_s^{OMI} and S_t^{OMI}), which are calculated from the stratospheric and

5   tropospheric AMFs (A_s^{OMI} and A_t^{OMI}) and VCDs (V_s^{OMI} and V_t^{OMI}) as follows:

6
$$S_{tot}^{OMI} = S_s^{OMI} + S_t^{OMI} = V_s^{OMI} \cdot A_s^{OMI} + V_t^{OMI} \cdot A_t^{OMI}. \tag{5}$$

7   Similarly, the bias-corrected OMI SCDs can be related to the OSIRIS stratospheric VCD

8   (V_s^{OSIRIS}) and the inferred (OmO) tropospheric VCD component (V_t^{OmO}), using the AMFs from

9   the OMI operational products:

10
$$S_{tot}^{OMI} \cdot \gamma = V_s^{OSIRIS} \cdot A_s^{OMI} + V_t^{OmO} \cdot A_t^{OMI}, \tag{6}$$

11   where γ is the OMI SCD bias correction factor described in Sect. 4.2. Solving for the OmO

12   VCD gives,

13
$$V_t^{OmO} = (\gamma \cdot S_{tot}^{OMI} - V_s^{OSIRIS} \cdot A_s^{OMI})/A_t^{OMI} \tag{7}$$

14   An alternate form, and the one used to compute the OmO product, is obtained by combining

15   Eq. (5) and Eq. (7):

16
$$V_t^{OmO} = \gamma \cdot V_t^{OMI} + (\gamma \cdot V_s^{OMI} - V_s^{OSIRIS}) \cdot A_s^{OMI}/A_t^{OMI} . \tag{8}$$

17   OmO tropospheric VCDs were computed using AMFs and VCDs from the OMI-SP product.

18   The ratio of air mass factors represents the different sensitivities to NO_2 located in the

19   troposphere and in the stratosphere. Typically, the ratio A_s^{OMI} / A_t^{OMI} is greater than one,

20   indicating that OMI is more sensitive to NO_2 within the stratosphere. OmO was not calculated

21   for the small number of OMI measurements for which the ratio $A_s^{OMI} / A_t^{OMI} > 15$, indicating

22   that the OMI measurement is not very sensitive to the troposphere. For each OMI pixel, V_s^{OSIRIS}

23   was interpolated from the OSIRIS gridded VCD maps (see Sect. 4.1) and γ was interpolated to

24   the OMI SCD (see Sect. 4.2).

25   **4.4   Matching of OSIRIS and OMI stratospheres**

26   Over unpolluted regions, the OmO tropospheric VCDs should be small and, subsequently, the

27   ($\gamma \cdot V_s^{OMI} - V_s^{OSIRIS}$) term in Eq. (8) should also be small. Therefore, the matching of the

28   OSIRIS and OMI stratospheres can be assessed by comparing OSIRIS stratospheric VCDs with

29   OMI VCDs scaled with γ, over unpolluted regions. Figure 8 shows annual average stratospheric

Atmospheric
Measurement
Techniques
Open Access
Discussions
EGU

1   VCDs for OMI-SP, OMI-DOMINO, and OSIRIS, binned by latitude over unpolluted regions

2   (OMI tropospheric VCDs $< 0.5 \times 10^{15}$ molecules/cm^2). Annual average OMI-SP and OMI-

3   DOMINO stratospheric VCDs are larger than OSIRIS VCDs by $\sim 0.6 \times 10^{15}$ for all latitudes.

4   When OMI-SP and OMI-DOMINO stratospheric VCDs are scaled with γ, agreement with

5   OSIRIS is to within 0.2×10^{15} molecules/cm^2 at all latitudes. This suggests that the OMI and

6   OSIRIS stratospheres are well-matched. Standard deviations over the year of the individual the

7   γ-scaled OMI VCDs are similar to OSIRIS VCDs at most latitudes. At 25°S, 35°S, and 55°N,

8   the standard deviation in the OSIRIS VCDs is larger than the standard deviation in the OMI-

9   SP or OMI-DOMINO VCDs.

10   OMI-SP, OMI-DOMINO and OSIRIS stratospheric VCD maps are shown for 4 March 2008 in

11   Figure 9. The OMI VCDs are larger than the OSIRIS VCDs, due to the high bias in the OMI

12   SCDs. There is somewhat less structure in the OSIRIS VCDs than in the OMI VCDs. For

13   example, OMI-DOMINO and OMI-SP stratospheric VCDs are enhanced across the northern

14   hemisphere Pacific and Mexico, but enhancements are not apparent in the OSIRIS data. There

15   is a large maximum in the OMI-DOMINO stratospheric VCDs over eastern China and Korea,

16   which is not apparent in the OMI-SP or OSIRIS VCDs. These features across the northern

17   hemisphere Pacific and Mexico, and over eastern China and Korea all persist in the OMI data

18   over the OSIRIS 3-day sampling period and cover a large enough area that they could be

19   resolved, although perhaps somewhat distorted, by the OSIRIS VCD maps. Therefore, these

20   local differences between the OSIRIS and OMI stratospheric VCDs cannot be attributed to the

21   smoothing and averaging of the OSIRIS measurements.

22   **4.5   OmO Tropospheric VCDs**

23   Figure 10 shows the OmO tropospheric VCDs, also for 4 March 2008. At most locations, OmO

24   VCDs are similar to the OMI-SP and OMI-DOMINO VCDs, with a few notable differences.

25   OmO VCDs are larger than OMI-SP and OMI-DOMINO VCDs over the northern hemisphere

26   Pacific and Mexico, which is consistent with the differences in the observed features in the

27   stratospheric VCDs. OmO VCDs are larger than OMI-DOMINO VCDs over eastern China

28   and Korea, as OmO effectively redistributes NO_2 from the stratosphere into the troposphere

29   through the second term in Eq. (8). Over much of India and China, OmO VCDs are smaller

30   than the OMI-SP VCDs.

Atmospheric
Measurement
Techniques
Discussions

1   Maps of annual average comparisons between OmO, OMI-SP, and OMI-DOMINO

2   tropospheric NO_2 are shown in Figure 11. Over unpolluted regions, differences between OmO

3   and the operational OMI data products are fairly small, suggesting that the matching of the

4   OSIRIS and OMI stratospheres was effective. OmO has less NO_2 than OMI-SP and OMI-

5   DOMINO over polluted regions such as the eastern United States, Europe, and eastern China.

6   This is expected as the OMI-SP and OMI-DOMINO tropospheric VCDs are biased high by

7   ~10-15% over polluted regions due to the bias in the SCDs (Marchenko et al., 2015). Over

8   Korea, both the OMI-SP and OmO VCDs are larger than the OMI-DOMINO VCDs. At

9   southern hemisphere midlatitudes, both the OmO and OMI-DOMINO VCDs are biased low

10   relative to OMI-SP VCDs. Overall, the differences between the OmO VCDs and the

11   operational OMI data products are within the range of the differences between the two

12   operational OMI data products.

13   Tropospheric VCDs over the Pacific Ocean can be used to assess the quality of the stratosphere-

14   troposphere separation because tropospheric VCDs are expected to be near background levels.

15   Figure 5 from Hilboll et al. (2013) shows climatological monthly mean tropospheric VCDs over

16   the Pacific (180°W to 150°W) binned according to month and latitude over 1998-2007, as

17   calculated from Oslo CTM2 model simulations (Søvde et al., 2008). At most latitudes,

18   tropospheric VCDs are $< 3 \times 10^{14}$ molecules/cm^2 according to the model results. For northern

19   hemisphere mid-latitudes, tropospheric VCDs are somewhat larger, ranging from ~2-7x10^{14}

20   molecules/cm^2, with the largest values at ~55°N in winter months.

21   Figure 12 shows monthly mean tropospheric VCDs from OMI-SP, OMI-DOMINO and OmO

22   over the Pacific (180°W to 150°W). The OMI-SP VCDs vary less with latitude and have no

23   mean negative values, unlike the OMI-DOMINO and OmO VCDs. This is expected as the

24   OMI-SP stratosphere-troposphere separation uses measurements over unpolluted regions,

25   including the Pacific, to estimate stratospheric NO_2. In the tropics, average VCDs from all

26   three datasets are $< 3 \times 10^{14}$ molecules/cm^2, which is consistent with background levels. At

27   northern hemisphere mid-latitudes, OmO mean VCDs increase slightly, ranging from ~2.5x10^{14}

28   to ~5x10^{14} molecules/cm^2. This is different from the OMI-SP and OMI-DOMINO VCDs,

29   which mostly remain $< 3 \times 10^{14}$ molecules/cm^2, but is consistent with the Oslo CTM2 model

30   simulations. At 55°N, both OmO and DOMINO mean VCDs are close to zero. In the southern

31   hemisphere, VCDs for all three datasets decrease with latitude, reaching values near 0

32   molecules/cm^2 in the OMI-SP and negative values in the OMI-DOMINO and OmO datasets at

Atmospheric
Measurement
Techniques
Discussions

1   45°S and 55°S. There are some large outliers in the OmO VCDs for April-July in the southern

2   hemisphere, suggesting a positive bias in the OmO dataset, likely because the OMI and OSIRIS

3   stratospheres were not well-matched (see Sect. 4.1). This is consistent with the observed

4   differences between OSIRIS and OMI-SP stratospheric VCDs for the same latitudes and

5   months. The standard deviations of the individual OmO and DOMINO tropospheric VCDs

6   over each month are also shown. All three datasets have smaller standard deviations in the

7   tropics and larger standard deviations toward mid-latitudes in both hemispheres. For the most-

8   part, the variability in the OmO VCDs is slightly smaller than the variability in the OMI-

9   DOMINO VCDs.

10   **4.6   Alternate OmO-DOMINO Tropospheric VCDs**

11   The OmO dataset is affected by the scaling of OSIRIS stratospheric VCDs to the OMI local

12   times, OMI SCD bias correction factor, the difference between the OMI and OSIRIS

13   stratospheres, and the choice of the OMI version of AMFs and VCDs (see Eq. (8)). In order to

14   gain some insight into the impact of these various terms in the OmO calculation, an alternate

15   OmO-DOMINO dataset was constructed using the OMI-DOMINO VCDs and AMFs (Figure

16   13). Over unpolluted regions, the OmO and OmO-DOMINO VCDs are very similar. Over

17   polluted areas, the OmO-DOMINO VCDs are somewhat larger than the OmO VCDs.

18   However, these differences are smaller in magnitude than the differences between the two OmO

19   products and the operational OMI data products (Figure 11 and Figure 13). The relative

20   contribution of the various terms in Eq. (8) on the OmO and OmO-DOMINO datasets are

21   discussed in the paragraphs below.

22   In order to match the OMI and OSIRIS stratospheres, both the OSIRIS and OMI datasets were

23   scaled prior to stratospheric subtraction. The OSIRIS stratospheric VCDs, measured in the

24   morning, were scaled to the OMI afternoon local time using a photochemical model, typically

25   increasing the OSIRIS stratospheric VCDs by ~0.5×10^{15} molecules/cm^2. The OMI SCD bias

26   correction factor was applied to OMI SCDs before creating the OmO and OmO-DOMINO

27   datasets. This correction factor is required in order to properly match the OMI and OSIRIS

28   stratospheres, for both the OMI-SP and OMI-DOMINO datasets (Figure 8). Without the

29   correction factor, both the OmO and OmO-DOMINO tropospheric VCDs would be very large

30   (~1×10^{15} molecules/cm^2) over the unpolluted Pacific Ocean. After the application of the diurnal

31   variation scaling and OMI SCD bias correction, the OMI-SP, OMI-DOMINO and OSIRIS

32   stratospheres VCDs agree to within ~0.2×10^{15} molecules/cm^2 on an annual average basis over

Atmospheric
Measurement
Techniques
Discussions

1　unpolluted areas (Figure 8). Furthermore, good overall matching of the stratosphere is

2　demonstrated by the OmO tropospheric VCDs over the Pacific Ocean (Figure 12). At specific

3　locations/times, the differences in the stratospheric VCDs can be much larger (Figure 9), but

4　this is difficult to quantify because of the role of the OMI SCD bias correction, which varies

5　according to the magnitude of the SCD. Therefore, the scaling of OSIRIS to the OMI local

6　time and the OMI SCD bias correction play similar and important roles for the both the OmO

7　and OmO-DOMINO datasets.

8　The OmO VCDs also depend on the ratio of AMFs (A_s/A_t), which scales the difference between

9　the OSIRIS and OMI stratospheric VCDs. Over unpolluted regions, this ratio is ~1.25 and is

10　nearly identical for both OMI-SP and OMI-DOMINO. Over polluted regions, the ratio is larger,

11　reaching annual averages of ~3-4 in some locations. Therefore, differences between OSIRIS

12　and OMI stratospheric VCDs are amplified over unpolluted areas through the dependence on

13　A_s/A_t in Eq. (8). Over polluted areas, A_s/A_t is somewhat smaller for OMI-SP than for OMI-

14　DOMINO, though the relationship is complicated because Eq. (8) also depends on the OMI

15　tropospheric VCDs, which also differ between the two operational OMI products, primarily

16　over polluted regions (Figure 11). This is consistent with the observed differences between the

17　OmO and OmO-DOMINO datasets, which are largest over polluted areas.

18　Overall, these tests suggest that the stratospheric matching between OSIRIS and OMI has a

19　larger influence on the OmO dataset than the choice of OMI AMFs. The stratospheric matching

20　currently depends on the OSIRIS and operational OMI stratospheric VCDs, as well as the OMI

21　SCD bias correction. Considering the complex manner in which biases in SCDs are transferred

22　into the OMI-SP and OMI-DOMINO stratospheric VCD, which can then affect unconstrained

23　(polluted) locations, it is impossible at this time to disentangle the impact of the SCD bias from

24　the larger issue of how well each method of stratospheric removal performs. Therefore, the

25　stratospheric matching between OSIRIS and OMI will be better understood once bias-corrected

26　OMI SCDs are available.

27

28　**5　Summary and Future Applications**

29　The technique of matching nadir- and limb-viewing satellite retrievals to quantify tropospheric

30　NO_2 is explored in this work using OMI nadir measurements and OSIRIS limb measurements

31　to create the OmO tropospheric NO_2 dataset. As nadir-viewing instruments cannot resolve NO_2

32　in the vertical, additional information or assumptions based on unpolluted regions are required

1   to determine quantities in the upper and lower atmospheric regions. Currently, there are two

2   operational products for OMI, which estimate stratospheric NO_2 using different methods. The

3   OMI-DOMINO product assimilates OMI SCDs into the TM4 model and then subtracts

4   modelled stratospheric NO_2. The OMI-SP dataset estimates stratospheric VCDs for locations

5   with background levels of tropospheric NO_2 and then uses an extrapolation technique to infer

6   stratospheric VCDs across the globe.

7   The new OmO tropospheric NO_2 dataset uses information from OSIRIS profile measurements

8   in order to estimate the stratospheric contribution to OMI SCD measurements. OSIRIS NO_2

9   stratospheric VCDs were found agree to within 0.25×10^{15} molecules/cm^2 of the SCIAMACHY,

10   HIRDLS, and MIPAS limb instruments for most latitudes and seasons (Appendix A). OSIRIS

11   profile measurements of stratospheric NO_2 were scaled to a range of local times using a

12   photochemical model. Stratospheric VCDs were calculated and were gridded onto daily maps

13   of stratospheric NO_2 for various local times. The OSIRIS VCD maps are averaged over a 3-

14   day window, in order to gain sufficient coverage from the OSIRIS measurements, which could

15   smooth out rapid variations in stratospheric NO_2, such as vortex intrusions. For each OMI

16   measurement, the OSIRIS VCD maps were interpolated to the latitude, longitude, and local

17   time of the OMI measurement. Then the OSIRIS stratospheric VCD and OMI-SP VCDs and

18   AMFs were used to calculate the OmO product for 60°S – 60°N. In order to match the OSIRIS

19   and OMI data products, corrections for a known bias in OMI SCDs were applied based on the

20   findings of Marchenko et al. (2015). After accounting for a bias in the OMI SCDs, the OSIRIS

21   and OMI annual average stratospheric VCDs agree to within 0.2×10^{15} molecules/cm^2 between

22   60°S and 60°N. Therefore, no additional corrections were applied to the data.

23   The OmO tropospheric VCDs reproduced the broad features of the OMI-SP and OMI-

24   DOMINO tropospheric VCDs. Furthermore, over the Pacific Ocean, the OmO VCDs were

25   consistent with background levels of NO_2 at most latitudes, suggesting that, overall, the

26   stratospheric NO_2 signal has been successfully removed using the OSIRIS dataset. There are

27   high biases in the OmO dataset for ~20°S-40°S in April – July, which are consistent with

28   observed systematic differences between the OSIRIS and OMI datasets for these latitudes and

29   months. Despite this, the matching of the OSIRIS and OMI stratospheres is very good given

30   the rudimentary nature of the OMI SCD-bias correction. No corrections were applied to

31   account for biases between the OSIRIS and OMI datasets. This differs from the technique of

32   Hilboll et al. (2013), who matched SCIAMACHY limb and nadir measurements through daily

1   corrections based on the comparisons over the Pacific Ocean. At present, errors remaining after

2   the simple OMI bias-correction cannot be separated from those in OSIRIS stratospheric VCD.

3   As such a more quantitative assessment of the potential of this approach can be made only once

4   the next version of OMI SCDs are available.

5   The results of this study show preliminary success in the compatibility of limb and nadir

6   measurements taken at different local times in a simpler framework.   This technique could be

7   improved by better accounting for biases between the OMI and OSIRIS datasets. For example,

8   in a full analysis, limb-measured stratospheric NO_2 and nadir-measured columns could be

9   assimilated together in a chemical transport model to estimate stratospheric NO_2.

10   This work underlines the challenge associated with matching polar orbiting, limb-viewing

11   instruments with future geostationary nadir-viewing instruments as the measurements occur at

12   many local solar times. By the end of the decade, three geostationary satellite instruments will

13   measure NO_2 in the nadir viewing geometry: the TROPOspheric Monitoring Instrument

14   (TROPOMI) (Veefkind et al., 2012) with coverage over Europe, the Tropospheric Emissions:

15   Monitoring of Pollution (TEMPO) (Zoogman et al., 2014) with coverage over North America,

16   and the Geostationary Environmental Monitoring Spectrometer (GEMS) (Kim, 2012) with

17   coverage over eastern Asia. While this study demonstrates that limb and nadir measurements

18   could be matched to retrieve tropospheric NO_2, there are currently no planned limb instruments

19   to overlap with these geostationary missions. OSIRIS is well-beyond its expected life-time and

20   there are no planned satellites that can measure stratospheric NO_2 beyond 2017, when the

21   Stratospheric Aerosol and Gas Experiment III (SAGE III) on the International Space Station

22   (ISS) reaches the end of its one-year design lifetime.

23

Atmospheric
Measurement
Techniques
Discussions

1 **Appendix A: Comparison of OSIRIS NO₂ to other satellite instruments**

2 In order to assess the OSIRIS v5 NO_2 product, OSIRIS data for 2005-2007 were compared

3 against the results of Belmonte Rivas et al. (2014). The study included limb satellite

4 measurements from MIPAS (IMK-IAA version 4.0; Funke et al., 2005), HIRDLS (version 7;

5 Gille et al., 2012), and SCIAMACHY (v3.1; Bauer et al., 2012), as well as satellite nadir

6 measurements from OMI (KNMI DOMINO version 2.0 Boersma et al., 2004, 2011) and

7 SCIAMACHY (KNMI-BIRA TM4NO2A version 2.3; Boersma et al., 2004). Belmonte Rivas

8 et al. (2014) found that the limb stratospheric VCDs from SCIAMACHY-limb, MIPAS, and

9 HIRDLS agree to within 0.25×10^{15} molecules/cm^2, which is better than 10%, when all

10 observations are adjusted to the HIRDLS local time. Nadir SCIAMACHY and OMI

11 stratospheric VCDs are biased relative to the limb instruments by -20% (-0.5×10^{15}

12 molecules/cm^2) and +20% (0.6×10^{15} molecules/cm^2), respectively.

13 OSIRIS profiles were averaged using the methodology of Belmonte Rivas et al. (2014).

14 OSIRIS profiles were scaled to the HRDLS local time of ~15:30 LT (Fig. 3 of Belmonte Rivas

15 et al., 2014), using the photochemical model described in Sect 2.3 and the methodology

16 described in Sect. 3.1. The photochemical model runs for the 2005-2007 OSIRIS profiles

17 presented here use the settings described by Brohede et al. (2008). Volume mixing ratio (VMR)

18 profiles were averaged daily in 2° latitude bins from 64°S to 80°N. Partial column profiles

19 $n_v(z_i)$ were calculated from the VMRs (V) using

20 $$n_{v(z_i)} = 10 \cdot N_A/(g \cdot M_{air}) \cdot 0.5 \cdot (V_{i+1} + V_i) \cdot (p_{i+1} - p_i) \qquad \text{(A1)}$$

21 where N_A is Avogadro's constant (6.022×10^{23} molecules/mole), g is the Earth's gravity (9.80

22 m/s^2), and M_{air} is the molar mass of air (28.97 g/mole). The pressure increments in hPa were

23 $p_i = 1000 \cdot 10^{-i/24}$ for i = 0–120. Belmonte Rivas et al. (2014) imposed collocation criteria as

24 well as some smoothing, which were not included here. Therefore, the comparisons presented

25 here are similar to the figures of Belmonte Rivas et al. (2014), but not identical.

26 Figure A1 shows OSIRIS partial column profiles versus latitude averaged over four seasons for

27 1 February 2005 – 31 Jan 2008. The OSIRIS profiles reproduce the altitude variation and

28 seasonality of the other datasets, shown in Fig. 6 of Belmonte Rivas et al. (2014) over the same

29 altitude range. Stratospheric VCDs were calculated from the OSIRIS partial column profiles

30 from the top altitude of the available measurements to 287 hPa. OSIRIS stratospheric VCDs

31 are shown in Fig. A2, alongside SCIAMACHY limb, MIPAS, HIRDLS, SCIAMACHY nadir,

Atmospheric
Measurement
Techniques
Open Access
EGU
Discussions

1   and OMI measurements. This figure is similar to Figure 8 of Belmonte Rivas et al. (2014).

2   OSIRIS stratospheric VCDs are within 0.25×10^{15} molecules/cm^2 of the other limb instruments

3   (SCIAMACHY-limb, MIPAS, and HIRDLS) for most latitudes and seasons. However, there

4   are some localized differences between all four limb instruments of $\sim 0.5 \times 10^{15}$ molecules/cm^2,

5   especially toward higher latitudes. These biases are not due to broad differences in sampling,

6   as similar differences are also observed in Figure 8 of Belmonte Rivas et al. (2014), where

7   collocation criteria were imposed. Therefore the localized differences between the limb

8   instruments are related to uncertainties in the measurements or the local time corrections.

9

Acknowledgements

18

Atmospheric
Measurement
Techniques
Discussions

1 **References**

2

3 Bauer, R., Rozanov, A., McLinden, C. A., Gordley, L. L., Lotz, W., Russell III, J. M., Walker,
4 K. A., Zawodny, J. M., Ladstätter-Weißenmayer, A., Bovensmann, H. and Burrows, J. P.:
5 Validation of SCIAMACHY limb NO_2 profiles using solar occultation measurements, Atmos.
6 Meas. Tech., 5, 1059–1084, doi:10.5194/amt-5-1059-2012, 2012.

7 Beirle, S., Kühl, S., Puķīte, J. and Wagner, T.: Retrieval of tropospheric column densities of
8 NO_2 from combined SCIAMACHY nadir/limb measurements, Atmos. Meas. Tech., 3, 283–
9 299, doi:10.5194/amt-3-283-2010, 2010.

10 Belmonte Rivas, M., Veefkind, P., Boersma, F., Levelt, P., Eskes, H. and Gille, J.:
11 Intercomparison of daytime stratospheric NO_2 satellite retrievals and model simulations,
12 Atmos. Meas. Tech., 7, 2203–2225, doi:10.5194/amt-7-2203-2014, 2014.

13 Belmonte Rivas, M., Veefkind, P., Eskes, H. and Levelt, P.: OMI tropospheric NO_2 profiles
14 from cloud slicing: Constraints on surface emissions, convective transport and lightning NO_x,
15 Atmos. Chem. Phys., 15, 13519–13553, doi:10.5194/acp-15-13519-2015, 2015.

16 Boersma, K. F., Eskes, H. J. and Brinksma, E. J.: Error analysis for tropospheric NO_2 retrieval
17 from space, J. Geophys. Res., 109, D04311, doi:10.1029/2003JD003962, 2004.

18 Boersma, K. F., Eskes, H. J., Veefkind, J. P., Brinksma, E. J., van der A, R. J., Sneep, M., van
19 der Oord, G. H. J., Levelt, P. F., Stammes, P., Gleason, J. F. and Bucsela, E. J.: Near-real time
20 retrieval of tropospheric NO_2 from OMI, Atmos. Chem. Phys., 7, 2103–2118, doi:10.5194/acp-
21 7-2103-2007, 2007.

22 Boersma, K. F., Eskes, H. J., Dirksen, R. J., Van Der A, R. J., Veefkind, J. P., Stammes, P.,
23 Huijnen, V., Kleipool, Q. L., Sneep, M., Claas, J., Leitão, J., Richter, A., Zhou, Y. and Brunner,
24 D.: An improved tropospheric NO_2 column retrieval algorithm for the Ozone Monitoring
25 Instrument, Atmos. Meas. Tech., 4, 1905–1928, doi:10.5194/amt-4-1905-2011, 2011.

26 Bovensmann, H., Burrows, J. P., Buchwitz, M., Frerick, J., Noël, S., Rozanov, V. V., Chance,
27 K. V. and Goede, A. P. H.: SCIAMACHY: Mission Objectives and Measurement Modes, J.
28 Atmos. Sci., 56(2), 127–150, doi:10.1175/1520-0469(1999)056<0127:SMOAMM>2.0.CO;2,
29 1999.

30 Brohede, S., McLinden, C. A., Urban, J., Haley, C. S., Jonsson, A. I. and Murtagh, D.: Odin
31 stratospheric proxy NO_y measurements and climatology, Atmos. Chem. Phys., 8, 5731–5754,
32 doi:10.5194/acp-8-5731-2008, 2008.

33 Brohede, S. M., Haley, C. S., McLinden, C. A., Sioris, C. E., Murtagh, D. P., Petelina, S. V.,
34 Llewellyn, E. J., Bazureau, A., Goutail, F., Randall, C. E., Lumpe, J. D., Taha, G., Thomasson,
35 L. W. and Gordley, L. L.: Validation of Odin/OSIRIS stratospheric NO_2 profiles, J. Geophys.
36 Res. Atmos., 112(D07310), 1–22, doi:10.1029/2006JD007586, 2007.

37 Bucsela, E. J., Celarier, E. A., Wenig, M. O., Gleason, J. F., Veefkind, J. P., Boersma, K. F.
38 and Brinksma, E. J.: Algorithm for NO_2 vertical column retrieval from the ozone monitoring
39 instrument, IEEE Trans. Geosci. Remote Sens., 44(5), 1245–1258,
40 doi:10.1109/TGRS.2005.863715, 2006.

41 Bucsela, E. J., Krotkov, N. A., Celarier, E. A., Lamsal, L. N., Swartz, W. H., Bhartia, P. K.,
42 Boersma, K. F., Veefkind, J. P., Gleason, J. F. and Pickering, K. E.: A new stratospheric and
43 tropospheric NO_2 retrieval algorithm for nadir-viewing satellite instruments: Applications to

Atmospheric
Measurement
Techniques
Open Access
Discussions
EGU

1   OMI, Atmos. Meas. Tech., 6, 2607–2626, doi:10.5194/amt-6-2607-2013, 2013.

2   Burrows, J. P., Weber, M., Buchwitz, M., Rozanov, V., Ladstätter-Weißenmayer, A., Richter,
3   A., DeBeek, R., Hoogen, R., Bramstedt, K., Eichmann, K.-U., Eisinger, M. and Perner, D.: The
4   Global Ozone Monitoring Experiment (GOME): Mission, instrument concept, and first
5   scientific   results,   J.   Atmos.   Sci.,   56(2),   151–175,   doi:10.1175/1520-
6   0469(1999)056<0151:TGOMEG>2.0.CO;2, 1999.

7   Callies, J., Corpaccioli, E., Eisinger, M., Hahne, A. and Lefebvre, A.: GOME-2 - Metop's
8   second-generation sensor for operational ozone monitoring, ESA Bull. Sp. Agency, 102, 28–
9   36, 2000.

10   Chance, K. V. and Spurr, R. D.: Ring effect studies: Rayleigh scattering, including molecular
11   parameters for rotational Raman scattering, and the Fraunhofer spectrum, Appl. Opt., 36(21),
12   5224–5230, doi:10.1364/AO.36.005224, 1997.

13   Chance, K. V., Liu, X., Suleiman, R. M., Flittner, D. E., Al-Saadi, J. and Janz, S. J.:
14   Tropospheric emissions: monitoring of pollution (TEMPO), in SPIE, vol. 8866, edited by J. J.
15   Butler, X. Xiong, and X. Gu, SPIE - International Society for Optical Engineering., 2013.

16   Choi, S., Joiner, J., Choi, Y., Duncan, B. N., Vasilkov, A., Krotkov, N. and Bucsela, E.: First
17   estimates of global free-tropospheric NO_2 abundances derived using a cloud-slicing technique
18   applied to satellite observations from the Aura Ozone Monitoring Instrument (OMI), Atmos.
19   Chem. Phys., 14, 10565–10588, doi:10.5194/acp-14-10565-2014, 2014.

20   Degenstein, D. A., Bourassa, A. E., Roth, C. Z. and Llewellyn, E. J.: Limb scatter ozone
21   retrieval from 10 to 60 km using a Multiplicative Algebraic Reconstruction Technique, Atmos.
22   Chem. Phys., 9, 6521–6529, doi:10.5194/acp-9-6521-2009, 2009.

23   Dirksen, R. J., Boersma, K. F., Eskes, H. J., Ionov, D. V., Bucsela, E. J., Levelt, P. F. and
24   Kelder, H. M.: Evaluation of stratospheric NO_2 retrieved from the Ozone Monitoring
25   Instrument: Intercomparison, diurnal cycle, and trending, J. Geophys. Res. Atmos.,
26   116(D08305), 1–22, doi:10.1029/2010JD014943, 2011.

27   Duncan, B. N., Lamsal, L. N., Thompson, A. M., Yoshida, Y., Lu, Z., Streets, D. G., Hurwitz,
28   M. M. and Pickering, K. E.: A space-based, high-resolution view of notable changes in urban
29   NO_2 pollution around the world (2004-2014), J. Geophys. Res., 121, 976–996, doi:10.1002/
30   2015JD024121, 2016.

31   Fischer, H., Birk, M., Blom, C., Carli, B., Carlotti, M., von Clarmann, T., Delbouille, L.,
32   Dudhia, A., Ehhalt, D., Endemann, M., Flaud, J. M., Gessner, R., Kleinert, A., Koopmann, R.,
33   Langen, J., López-Puertas, M., Mosner, P., Nett, H., Oelhaf, H., Perron, G., Remedios, J.,
34   Ridolfi, M., Stiller, G. and Zander, R.: MIPAS: an instrument for atmospheric and climate
35   research, Atmos. Chem. Phys., 8, 2151–2188, doi:10.5194/acp-8-2151-2008, 2008.

36   Funke, B., López-Puertas, M., von Clarmann, T., Stiller, G. P., Fischer, H., Glatthor, N.,
37   Grabowski, U., Höpfner, M., Kellmann, S., Kiefer, M., Linden, A., Mengistu Tsidu, G., Milz,
38   M., Steck, T. and Wang, D. Y.: Retrieval of stratospheric NO_x from 5.3 and 6.2 μm nonlocal
39   thermodynamic equilibrium emissions measured by Michelson Interferometer for Passive
40   Atmospheric   Sounding   (MIPAS)   on   Envisat,   J.   Geophys.   Res.,   110,   D09302,
41   doi:10.1029/2004JD005225, 2005.

42   Gille, J., Barnett, J., Arter, P., Barker, M., Bernath, P., Boone, C., Cavanaugh, C., Chow, J.,
43   Coffey, M., Craft, J., Craig, C., Dials, M., Dean, V., Eden, T., Edwards, D. P., Francis, G.,
44   Halvorson, C., Harvey, L., Hepplewhite, C., Khosravi, R., Kinnison, D., Krinsky, C., Lambert,
45   A., Lee, H., Lyjak, L., Loh, J., Mankin, W., Massie, S., McInerney, J., Moorhouse, J., Nardi,

Atmospheric
Measurement
Techniques
Discussions

Open Access

B., Packman, D., Randall, C., Reburn, J., Rudolf, W., Schwartz, M., Serafin, J., Stone, K., Torpy, B., Walker, K., Waterfall, A., Watkins, R., Whitney, J., Woodard, D. and Young, G.: High Resolution Dynamics Limb Sounder: Experiment overview, recovery, and validation of initial temperature data, J. Geophys. Res. Atmos., 113(D16S43), 1–23, doi:10.1029/2007JD008824, 2008.

Gille, J., Cavanaugh, C., Halvorson, C., Hartsough, C., Nardi, B., Rivas, M., Khosravi, R., Smith, L. and Francis, G.: Final correction algorithms for HIRDLS version 7 data, Proc. SPIE, 8511, 85110K, doi:10.1117/12.930175, 2012.

Haley, C. S. and Brohede, S.: Status of the Odin/OSIRIS stratospheric O_3 and NO_2 data products, Can. J. Phys., 85(11), 1177–1194, doi:10.1139/P07-114, 2007.

Hendrick, F., Van Roozendael, M., Kylling, A., Petritoli, A., Rozanov, A., Sanghavi, S., Schofield, R., von Friedeburg, C., Wagner, T., Wittrock, F., Fonteyn, D. and De Mazière, M.: Intercomparison exercise between different radiative transfer models used for the interpretation of ground-based zenith-sky and multi-axis DOAS observations, Atmos. Chem. Phys., 6, 93–108, doi:10.5194/acp-6-93-2006, 2006.

Hilboll, A., Richter, A., Rozanov, A., Hodnebrog, Ø., Heckel, A., Solberg, S., Stordal, F. and Burrows, J. P.: Improvements to the retrieval of tropospheric NO_2 from satellite - Stratospheric correction using SCIAMACHY limb/nadir matching and comparison to Oslo CTM2 simulations, Atmos. Meas. Tech., 6, 565–584, doi:10.5194/amt-6-565-2013, 2013.

Ingmann, P., Veihelmann, B., Langen, J., Lamarre, D., Stark, H. and Courrèges-Lacoste, G. B.: Requirements for the GMES Atmosphere Service and ESA's implementation concept: Sentinels-4/-5 and -5p, Remote Sens. Environ., 120, 58–69, doi:10.1016/j.rse.2012.01.023, 2012.

Jonsson, A. I., de Grandpré, J., Fomichev, V. I., McConnell, J. C. and Beagley, S. R.: Doubled CO_2-induced cooling in the middle atmosphere: Photochemical analysis of the ozone radiative feedback, J. Geophys. Res., 109, D24103, doi:10.1029/2004JD005093, 2004.

Kalnay, E., Kanamisu, M., Kistler, R., Collins, W., Deaven, D., Gandin, L., Iredell, M., Saha, S., White, G., Woollen, J., Zhu, Y., Chelliah, M., Ebisuzaki, W., Higgins, W., Janowiak, J., Mo, K. C., Ropelewski, C., Wang, J., Leetmaa, A., Reynolds, R., Jenne, R. and Dennis, J.: The NCEP/NCAR 40 Year Reanalysis Project, Bull. Am. Meteorol. Soc., 77, 437–471, doi:http://dx.doi.org/10.1175/1520-0477(1996)077<0437:TNYRP>2.0.CO;2, 1996.

Kerzenmacher, T., Wolff, M. A., Strong, K., Dupuy, E., Walker, K. A., Amekudzi, L. K., Batchelor, R. L., Bernath, P. F., Berthet, G., Blumenstock, T., Boone, C. D., Bramstedt, K., Brogniez, C., Brohede, S., Burrows, J. P., Catoire, V., Dodion, J., Drummond, J. R., Dufour, D. G., Funke, B., Fussen, D., Goutail, F., Griffith, D. W. T., Haley, C. S., Hendrick, F., Höpfner, M., Huret, N., Jones, N., Kar, J., Kramer, I., Llewellyn, E. J., López-Puertas, M., Manney, G., McElroy, C. T., McLinden, C. A., Melo, S., Mikuteit, S., Murtagh, D., Nichitiu, F., Notholt, J., Nowlan, C., Piccolo, C., Pommereau, J.-P., Randall, C., Raspollini, P., Ridolfi, M., Richter, A., Schneider, M., Schrems, O., Silicani, M., Stiller, G. P., Taylor, J., Tétard, C., Toohey, M., Vanhellemont, F., Warneke, T., Zawodny, J. M. and Zou, J.: Validation of NO_2 and NO from the Atmospheric Chemistry Experiment (ACE), Atmos. Chem. Phys., 8, 5801–5841, doi:10.5194/acp-8-5801-2008, 2008.

Kim, J.: GEMS(Geostationary Environment Monitoring Spectrometer) onboard the GeoKOMPSAT to Monitor Air Quality in high Temporal and Spatial Resolution over Asia-Pacific Region, EGU Gen. Assem. [online] Available from: http://adsabs.harvard.edu/abs/2012EGUGA..14.4051K (Accessed 12 April 2016), 2012.

Atmospheric
Measurement
Techniques
Discussions

Open Access

EGU

1   Krotkov, N. A., McLinden, C. A., Li, C., Lamsal, L. N., Celarier, E. A., Marchenko, S. V.,
2   Swartz, W. H., Bucsela, E. J., Joiner, J., Duncan, B. N., Boersma, K. F., Veefkind, J. P., Levelt,
3   P. F., Fioletov, V. E., Dickerson, R. R., He, H., Lu, Z. and Streets, D. G.: Aura OMI
4   observations of regional SO_2 and NO_2 pollution changes from 2005 to 2015, Atmos. Chem.
5   Phys., accepted, doi:10.5194/acpd-15-26555-2015, 2016.

6   Lamsal, L. N., Krotkov, N. A., Celarier, E. A., Swartz, W. H., Pickering, K. E., Bucsela, E. J.,
7   Gleason, J. F., Martin, R. V., Philip, S., Irie, H., Cede, A., Herman, J., Weinheimer, A.,
8   Szykman, J. J. and Knepp, T. N.: Evaluation of OMI operational standard NO_2 column
9   retrievals using in situ and surface-based NO_2 observations, Atmos. Chem. Phys., 14, 11587–
10 11609, doi:10.5194/acp-14-11587-2014, 2014.

11 Levelt, P. F., Van den Oord, G. H. J., Dobber, M. R., Mälkki, A., Visser, H., de Vries, J.,
12 Stammes, P., Lundell, J. O. V. and Saari, H.: The ozone monitoring instrument, IEEE Trans.
13 Geosci. Remote Sens., 44(5), 1093–1101, doi:10.1109/TGRS.2006.872333, 2006.

14 Llewellyn, E. J., Lloyd, N. D., Degenstein, D. A., Gattinger, R. L., Petelina, S. V., Bourassa,
15 A. E., Wiensz, J. . T., Ivanov, E. V., McDade, I. C., Solheim, B. H., McConnell, J. C., Haley,
16 C. S., von Savigny, C., Sioris, C. E., McLinden, C. A., Griffioen, E., Kaminski, J., Evans, W.
17 F. J., Puckrin, E., Strong, K., Wehrle, V., Hum, R. H., Kendall, D. J. W., Matsushita, J.,
18 Murtagh, D. P., Brohede, S., Stegman, J., Witt, G., Barnes, G., Payne, W. F., Piché, L., Smith,
19 K., Warshaw, G., Deslauniers, D.-L., Marchand, P., Richardson, E. H., King, R. A., Wevers, I.,
20 McCreath, W., Kyrölä, E., Oikarinen, L., Leppelmeier, G. W., Auvinen, H., Mégie, G.,
21 Hauchecorne, A., Lefèvre, F., de La Nöe, J., Ricaud, P., Frisk, U., Sjoberg, F., von Schéele, F.
22 and Nordh, L.: The OSIRIS instrument on the Odin spacecraft, Can. J. Phys., 82, 411–422,
23 doi:10.1139/p04-005, 2004.

24 Marchenko, S., Krotkov, N. A., Lamsal, L. N., Celarier, E. A., Swartz, W. H. and Bucsela, E.
25 J.: Revising the slant column density retrieval of nitrogen dioxide observed by the Ozone
26 Monitoring Instrument, J. Geophys. Res. Atmos., 120(11), 1–23, doi:10.1002/2014JD022913,
27 2015.

28 Martin, R. V., Chance, K., Jacob, D. J., Kurosu, T. P., Spurr, R. J. D., Bucsela, E., Gleason, J.
29 F., Palmer, P. I., Bey, I., Fiore, A. M., Li, Q., Yantosca, R. M. and Koelemeijer, R. B. A.: An
30 improved retrieval of tropospheric nitrogen dioxide from GOME, J. Geophys. Res. Atmos.,
31 107(D20), doi:10.1029/2001JD001027, 2002.

32 McLinden, C. A., Olsen, S. C., Hannegan, B., Wild, O., Prather, M. J. and Sundet, J.:
33 Stratospheric ozone in 3-D models: A simple chemistry and the cross-tropopause flux, J.
34 Geophys. Res., 105(D11), 14653–14665, doi:10.1029/2000JD900124, 2000.

35 McLinden, C. A., Haley, C. S. and Sioris, C. E.: Diurnal effects in limb scatter observations, J.
36 Geophys. Res. Atmos., 111(D14302), 1–10, doi:10.1029/2005JD006628, 2006.

37 McLinden, C. A., Fioletov, V., Boersma, K. F., Krotkov, N., Sioris, C. E., Veefkind, J. P. and
38 Yang, K.: Air quality over the Canadian oil sands: A first assessment using satellite
39 observations, Geophys. Res. Lett., 39(L04804), 1–8, doi:10.1029/2011GL050273, 2012a.

40 McLinden, C. A., Bourassa, A. E., Brohede, S., Cooper, M., Degenstein, D. A., Evans, W. J.
41 F., Gattinger, R. L., Haley, C. S., Llewellyn, E. J., Lloyd, N. D., Loewen, P., Martin, R. V.,
42 McConnell, J. C., McDade, I. C., Murtagh, D., Rieger, L., Von Savigny, C., Sheese, P. E.,
43 Sioris, C. E., Solheim, B. and Strong, K.: Osiris: A Decade of scattered light, Bull. Am.
44 Meteorol. Soc., 93, 1845–1863, doi:10.1175/BAMS-D-11-00135.1, 2012b.

45 Murtagh, D., Frisk, U., Merino, F., Ridal, M., Jonsson, A., Stegman, J., Witt, G., Eriksson, P.,
46 Jiménez, C., Megie, G., Noë, J. D. La, Ricaud, P., Baron, P., Pardo, J. R., Hauchecorne, A.,

Llewellyn, E. J., Degenstein, D. A., Gattinger, R. L., Lloyd, N. D., Evans, W. F. J., McDade, I. C., Haley, C. S., Sioris, C., von Savigny, C., Solheim, B. H., McConnell, J. C., Strong, K., Richardson, E. H., Leppelmeier, G. W., Kyrölä, E., Auvinen, H. and Oikarinen, L.: An overview of the Odin atmospheric mission, Can. J. Phys., 80, 309–319, doi:10.1139/p01-157, 2002.

Prather, M.: Catastrophic loss of stratospheric ozone in dense volcanic clouds, J. Geophys. Res., 97(D9), 10187–10191, doi:10.1029/92JD00845, 1992.

Richter, A. and Burrows, J. P.: Tropospheric NO_2 from GOME measurements, Adv. Sp. Res., 29(11), 1673–1683, doi:10.1016/S0273-1177(02)00100-X, 2002.

Richter, A., Burrows, J. P., Nüß, H., Granier, C. and Niemeier, U.: Increase in tropospheric nitrogen dioxide over China observed from space, Nat. Lett., 437, 129–132, doi:10.1038/nature04092, 2005.

Rieger, L. A., Bourassa, A. E. and Degenstein, D. A.: Merging the OSIRIS and SAGE II stratospheric aerosol records, J. Geophys. Res., 12(17), 1–15, doi:10.1002/2015JD023133, 2015.

Russell, A. R., Valin, L. C. and Cohen, R. C.: Trends in OMI NO_2 observations over the United States: Effects of emission control technology and the economic recession, Atmos. Chem. Phys., 12, 12197–12209, doi:10.5194/acp-12-12197-2012, 2012.

Schoeberl, M. R., Douglass, A. R., Hilsenrath, E., Bhartia, P. K., Beer, R., Waters, J. W., Gunson, M. R., Froidevaux, L., Gille, J. C., Barnett, J. J., Levelt, P. F. and DeCola, P.: Overview of the EOS aura mission, IEEE Trans. Geosci. Remote Sens., 44(5), 1066–1072, doi:10.1109/TGRS.2005.861950, 2006.

Scinocca, J. F., McFarlane, N. A., Lazare, M., Li, J. and Plummer, D.: The CCCma third generation AGCM and its extension into the middle atmosphere, Atmos. Chem. Phys., 8, 7055–7074, doi:10.5194/acp-8-7055-2008, 2008.

Sierk, B., Richter, A., Rozanov, A., Von Savigny, C., Schmoltner, A. M., Buchwitz, M., Bovensmann, H. and Burrows, J. P.: Retrieval and monitoring of atmospheric trace gas concentrations in nadir and limb geometry using the space-borne SCIAMACHY instrument, Environ. Monit. Assess., 120, 65–77, doi:10.1007/s10661-005-9049-9, 2006.

Sioris, C. E., Kurosu, T. P., Martin, R. V. and Chance, K.: Stratospheric and tropospheric NO_2 observed by SCIAMACHY: First results, Adv. Sp. Res., 34, 780–785, doi:10.1016/j.asr.2003.08.066, 2004.

Søvde, O. A., Gauss, M., Smyshlyaev, S. P. and Isaksen, I. S. A.: Evaluation of the chemical transport model Oslo CTM2 with focus on arctic winter ozone depletion, J. Geophys. Res., 113, D09304, doi:10.1029/2007JD009240, 2008.

van Geffen, J. H. G. M., Boersma, K. F., Van Roozendael, M., Hendrick, F., Mahieu, E., De Smedt, I., Sneep, M. and Veefkind, J. P.: Improved spectral fitting of nitrogen dioxide from OMI in the 405–465 nm window, Atmos. Meas. Tech., 8, 1685–1699, doi:10.5194/amt-8-1685-2015, 2015.

Veefkind, J. P., Boersma, K. F., Wang, J., Kurosu, T. P., Krotkov, N., Chance, K. and Levelt, P. F.: Global satellite analysis of the relation between aerosols and short-lived trace gases, Atmos. Chem. Phys., 11, 1255–1267, doi:10.5194/acp-11-1255-2011, 2011.

Veefkind, J. P., Aben, I., McMullan, K., Förster, H., de Vries, J., Otter, G., Claas, J., Eskes, H. J., de Haan, J. F., Kleipool, Q., van Weele, M., Hasekamp, O., Hoogeveen, R., Landgraf, J., Snel, R., Tol, P., Ingmann, P., Voors, R., Kruizinga, B., Vink, R., Visser, H. and Levelt, P. F.:

Atmospheric
Measurement
Techniques
Discussions

Open Access

EGU

1   TROPOMI on the ESA Sentinel-5 Precursor: A GMES mission for global observations of the
2   atmospheric composition for climate, air quality and ozone layer applications, Remote Sens.
3   Environ., 120, 70–83, doi:10.1016/j.rse.2011.09.027, 2012.

4   Zhou, Y., Brunner, D., Hueglin, C., Henne, S. and Staehelin, J.: Changes in OMI tropospheric
5   NO_2 columns over Europe from 2004 to 2009 and the influence of meteorological variability,
6   Atmos. Environ., 46, 482–495, doi:10.1016/j.atmosenv.2011.09.024, 2012.

7   Zoogman, P., Jacob, D. J., Chance, K., Liu, X., Lin, M., Fiore, A. and Travis, K.: Monitoring
8   high-ozone events in the US Intermountain West using TEMPO geostationary satellite
9   observations, Atmos. Chem. Phys., 14, 6261–6271, doi:10.5194/acp-14-6261-2014, 2014.

10

11

Atmospheric
Measurement
Techniques
Discussions

Open Access

1 **Tables**

2

3 **Table 1: Correction factors, γ, applied to the OMI SCDs as a function of the OMI SCD.**

4 **Correction factors are from Marchenko et al. (2015) and account for the high bias in the**

5 **OMI SCDs.**

SCD $\times 10^{16}$ molecules/cm^2	γ
0.5755	0.7645
0.8518	0.8049
1.2147	0.8152
1.7336	0.8475
2.3842	0.8721
3.3740	0.8912
4.4346	0.9017
5.4794	0.9082
6.4403	0.9169
7.5376	0.9218

6

7

8

1 **Figures**

2
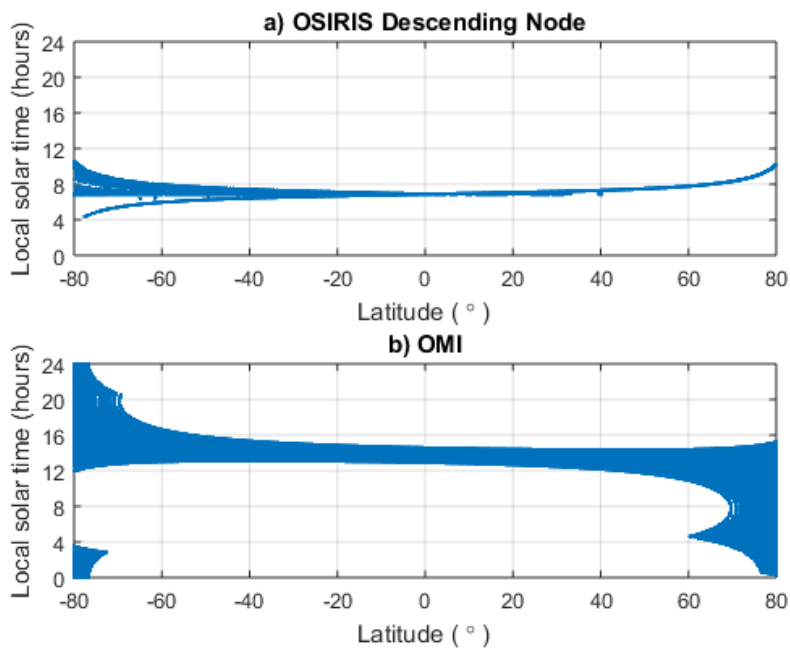
3

4 **Figure 1: Local solar time versus latitude for (a) OSIRIS descending node and (b) OMI**

5 **measurements in 2008. OSIRIS local times are for all profiles in 2008. OMI local times**

6 **are sampled for one day in each month.**
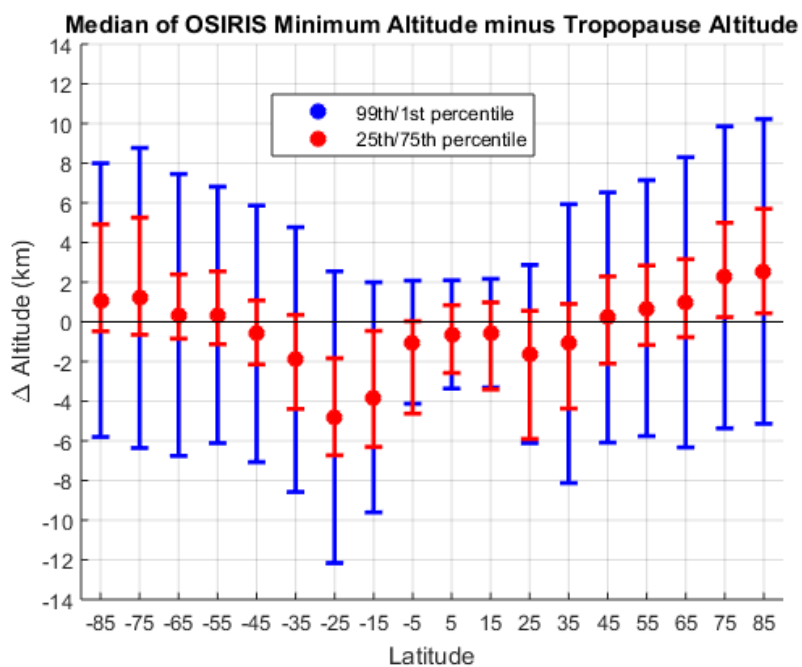
Figure 2: Difference between OSIRIS minimum measurement altitude and the tropopause altitude. Median and percentiles (red: 1ˢᵗ and 99ᵗʰ, blue: 25ᵗʰ and 5ᵗʰ) are shown within 10° latitude bins. Altitude differences < 0 indicate that OSIRIS profiles extended below the tropopause. Altitude differences > 0 indicate that OSIRIS profiles terminated above the tropopause.

Atmospheric
Measurement
Techniques
Discussions

Open Access

1
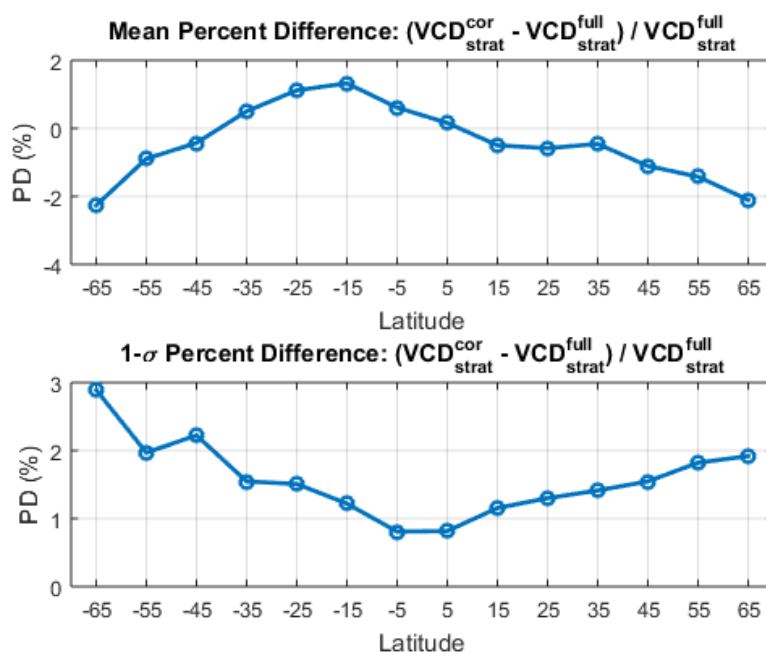
Figure 3: Effect of model scaling of OSIRIS partial VCDs for OSIRIS profiles that
terminate ~3-4 km above the thermal tropopause. (a) Mean and (b) 1-sigma of percent
difference of VCD$_{strat}^{cor}$ minus VCD$_{strat}^{full}$ within 10° latitude bins.

5

Atmospheric
Measurement
Techniques
Discussions

1
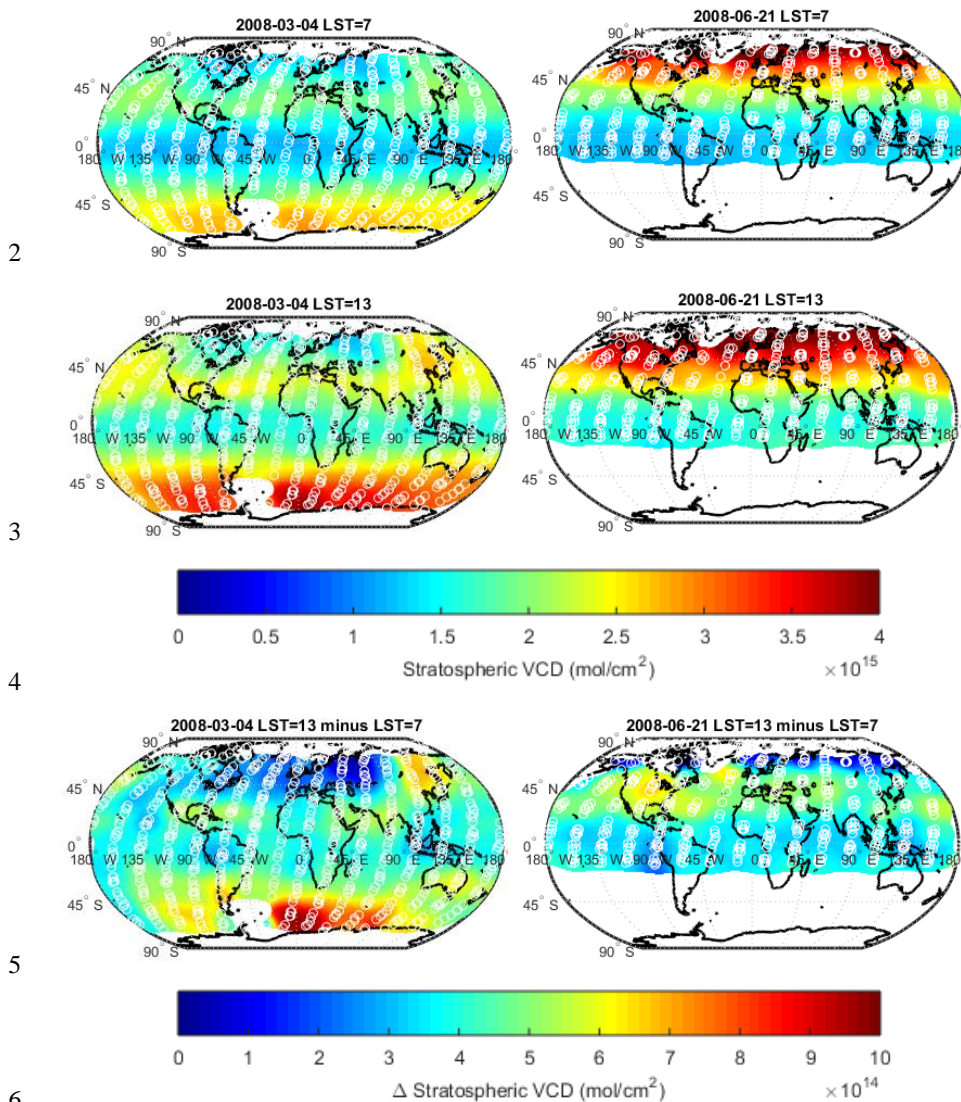
Figure 4: **OSIRIS stratospheric VCD maps for 4 March 2008 (left panels) and 21 June 2008 (right panels). The maps are shown for LST = 07:00 (top panels), corresponding to the approximate OSIRIS measurement time, and LST = 13:00 (middle panels), corresponding to the approximate OMI measurement time. Difference maps for LST = 13:00 minus 07:00 (bottom panels) are also shown. The white circles indicate the locations of the OSIRIS measurements used to create the maps.**

13

Atmospheric
Measurement
Techniques
Discussions

Open Access

1
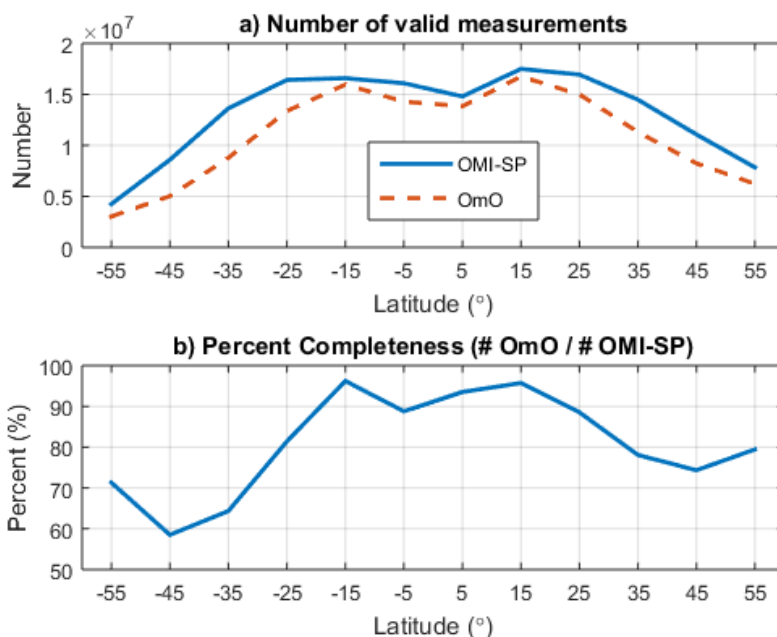
Figure 5: (a) Number of valid measurements for OMI-SP (blue line) and for OmO (red

dashed line). (b) Percent completeness of the OmO-SP dataset (number of valid OmO

measurements / number of valid OMI-SP measurements). Statistics were calculated in

10° latitude bins.

6

Atmospheric
Measurement
Techniques
Discussions

Open Access

1
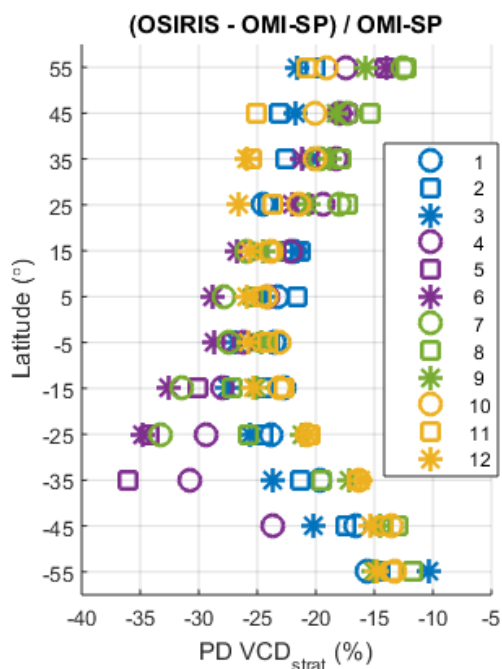
Figure 6: Percent difference of OSIRIS minus OMI-SP stratospheric VCDs (x-axis),

binned according to latitude (y-axis) and month (legend).

1
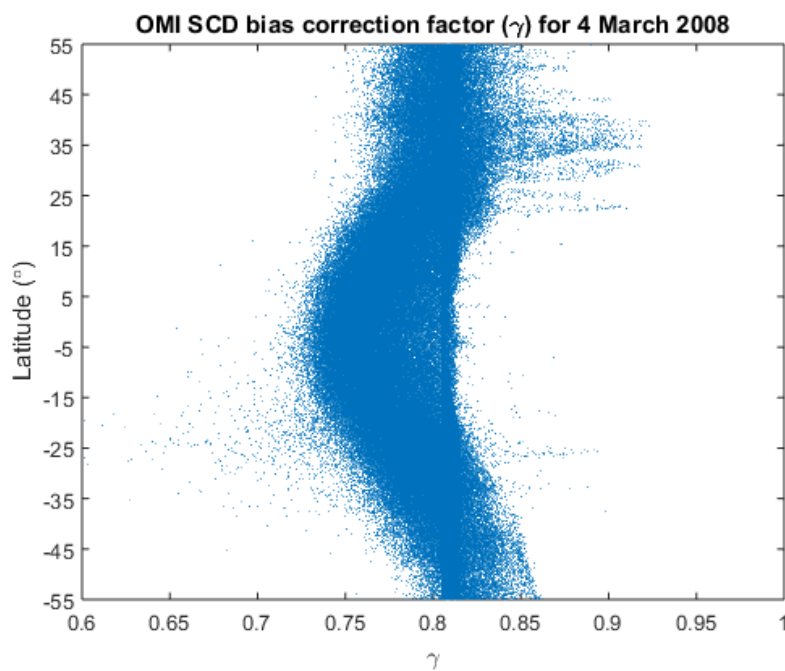
Figure 7: OMI SCD bias correction factors versus latitude for OMI-SP measurements on

4 March 2008.

4

5

1
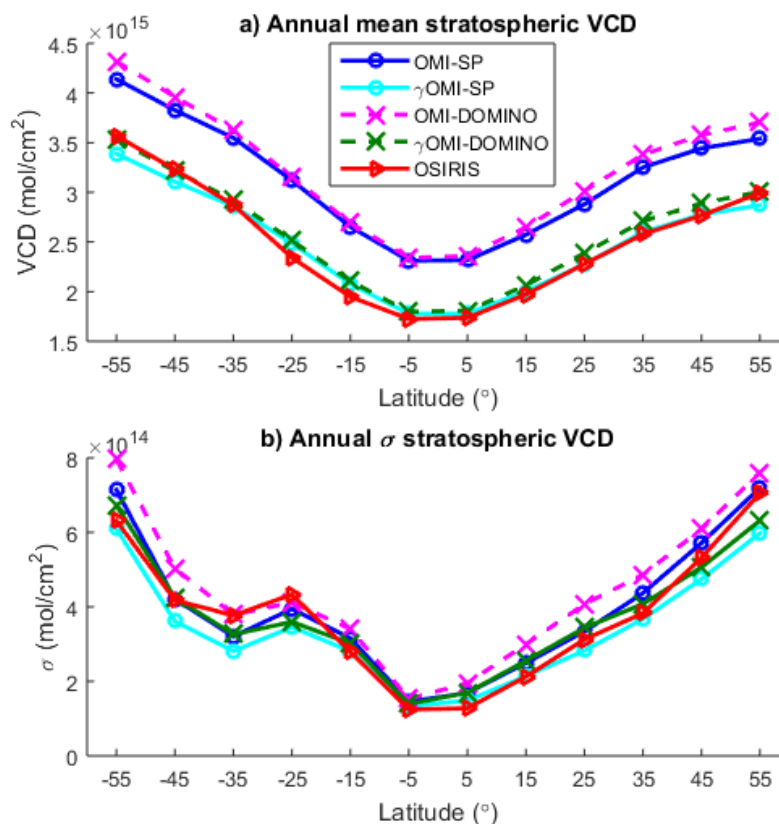
Figure 8: Annual (a) mean and (b) standard deviation of stratospheric VCDs for 2008 in

10° latitude bins for measurements with OMI tropospheric VCDs < 0.5x10^{15}

molecules/cm^2. Stratospheric VCDs for OMI-SP (blue circles), OMI-SP scaled by γ

(cyan circles), OMI-DOMINO (magenta X's), OMI-DOMINO scaled by γ (green X's),

and OSIRIS VCD maps interpolated to the OMI measurement time/location (red

triangles) are shown. Mean and standard deviation are calculated over individual OMI

measurements for the entire year.

Atmospheric
Measurement
Techniques
Discussions

1

2

3
4
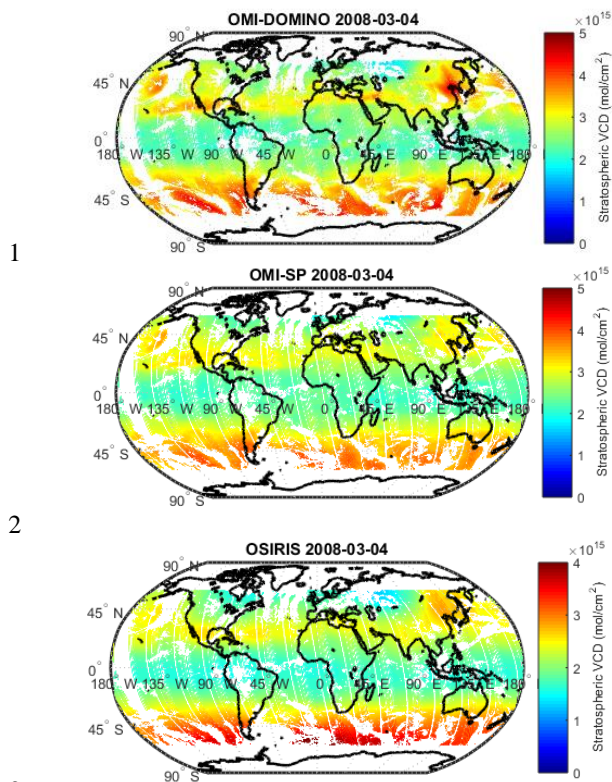
5 **Figure 9: Maps of stratospheric VCDs for 4 March 2008 for OMI-SP (top), OMI-**

6 **DOMINO (middle) and OSIRIS interpolated to the location of OMI measurements**

7 **(bottom). Note that different color scales are used for the OMI and OSIRIS VCDs.**

8

1

2

3

4
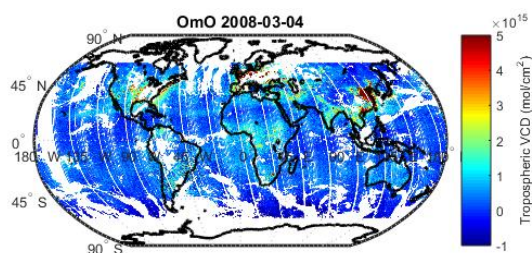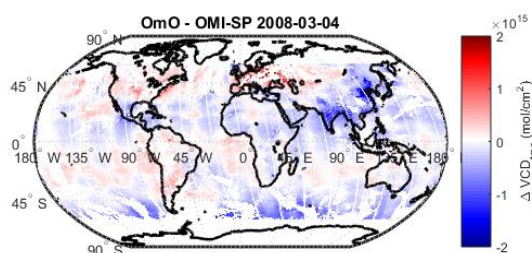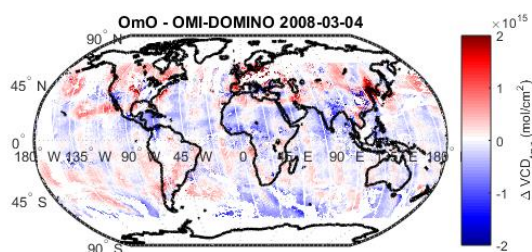
Figure 10: Maps of tropospheric VCDs for 4 March 2008 for OmO (top), the difference between OmO and OMI-SP (middle), and the difference between OmO and OMI-DOMINO (bottom).

8

Atmospheric
Measurement
Techniques
Discussions

1

2

3

4
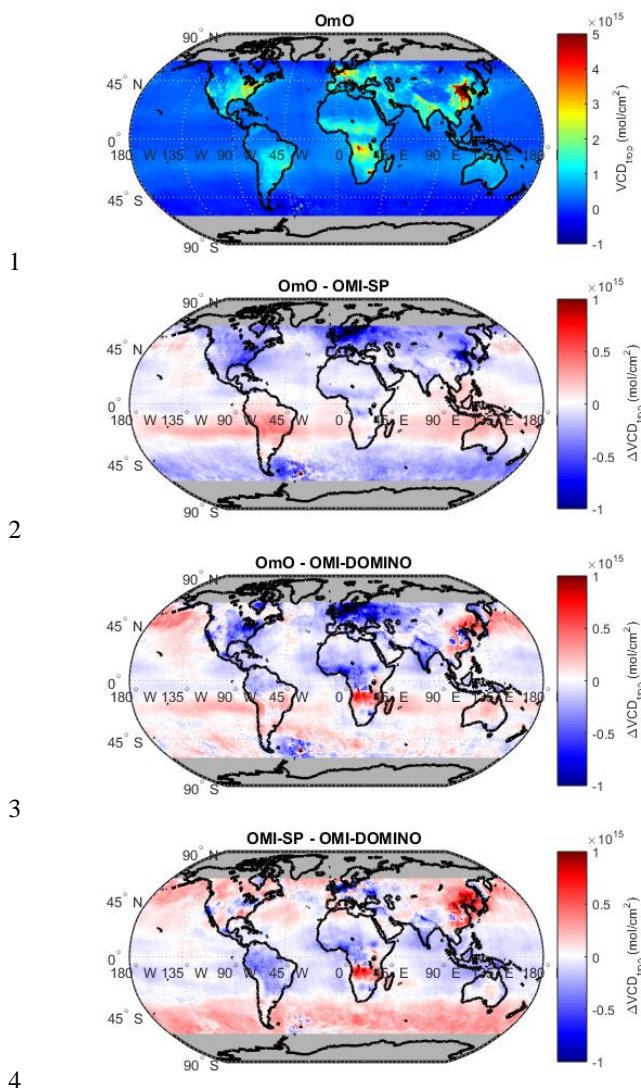
**Figure 11: Maps of annual average (top) OmO tropospheric VCDs and differences
between tropospheric VCDs for (top-middle) OmO minus OMI-SP, (bottom-middle)
OmO minus OMI-DOMINO, and (bottom) OMI-SP minus OMI-DOMINO. Maps are
averaged on a 1°x1° grid.**

9

10

Atmospheric
Measurement
Techniques
Discussions
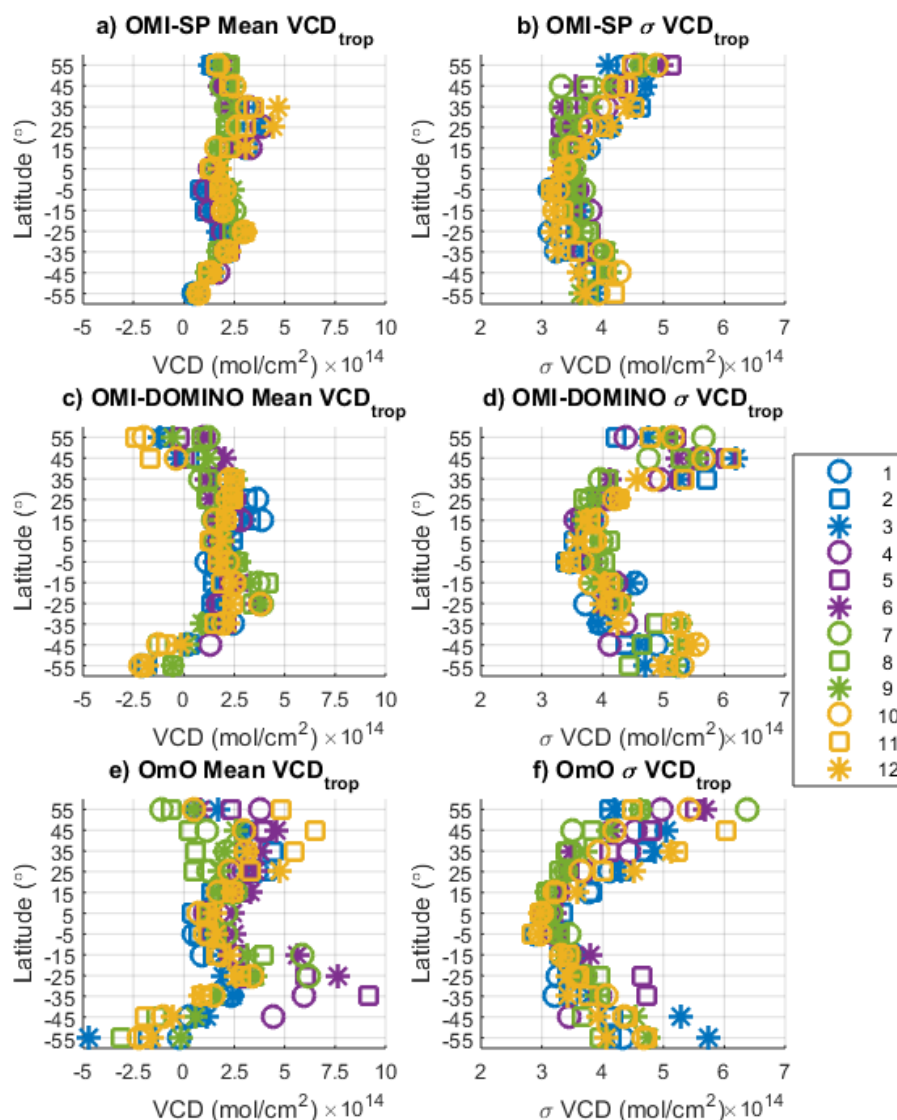
1

2 **Figure 12: Mean and standard deviation of VCDs in the Pacific (150°W to 180°W),**

3 **calculated monthly (legend) in 10° latitude bins. (a) OMI-SP mean VCD, (b) OMI-SP**

4 **standard deviation of VCD, (c) OMI-DOMINO mean VCD, (d) OMI-DOMINO**

5 **standard deviation of VCD, (e) OmO mean VCD, and (f) OmO standard deviation of**

6 **VCD.**

7

8

Atmospheric
Measurement
Techniques

Open Access

EGU

Discussions

1

2

3
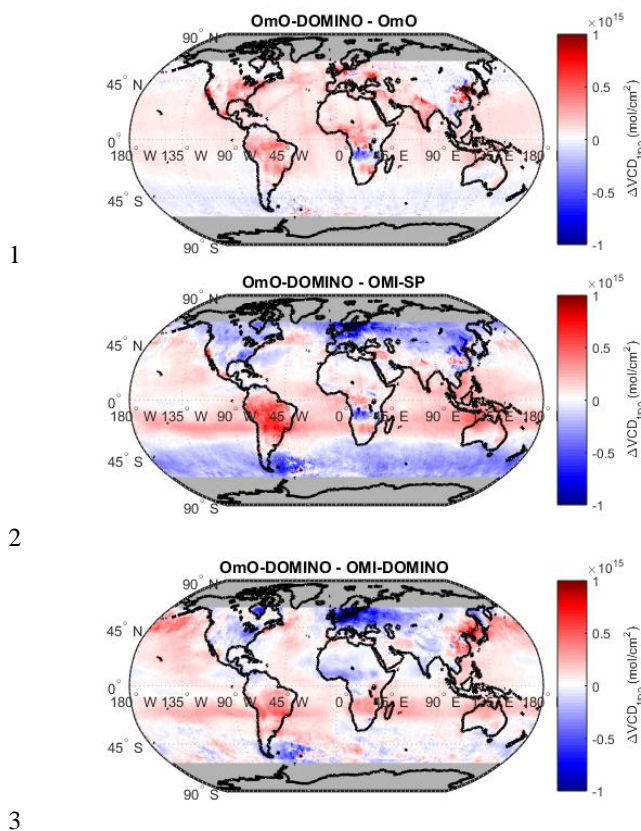
Figure 13: Maps of differences between OmO-DOMINO and (top) OmO, (middle) OMI-SP, and (bottom) OMI-DOMINO annual average tropospheric VCDs. Map is averaged on a 1x1° grid.

4

5

6

7

8

Atmospheric
Measurement
Techniques
Discussions

1
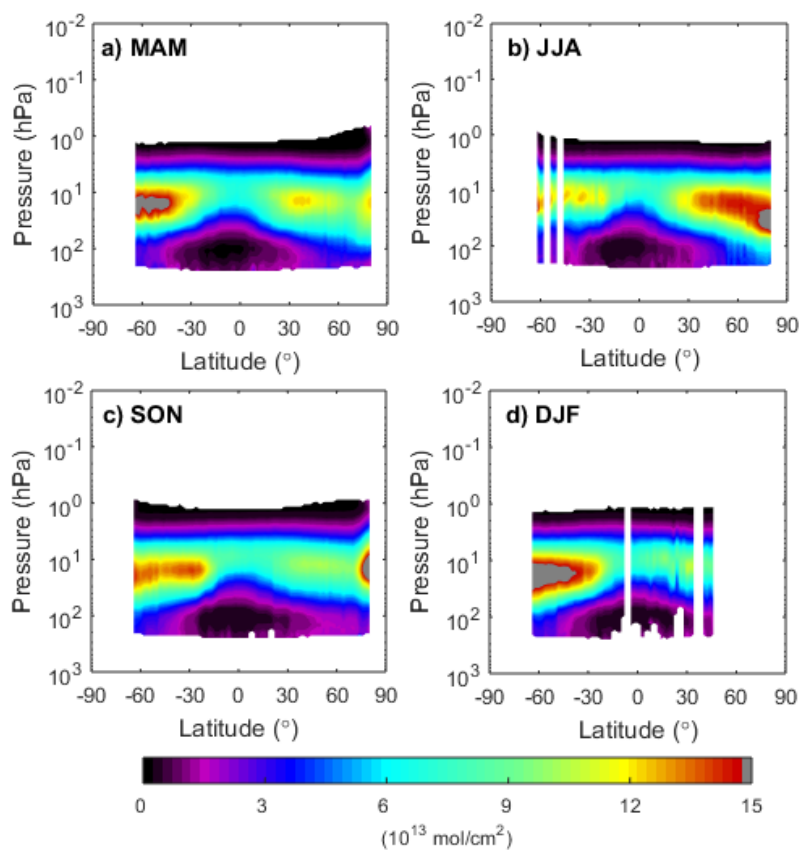
Figure A1. OSIRIS seasonal mean NO₂ partial column profiles in 2° latitude bins for (a)

March-April-May (MAM), (b) June-July-August (JJA), (c) September-October-

November (SON) and (d) December-January-February (DJF).

1
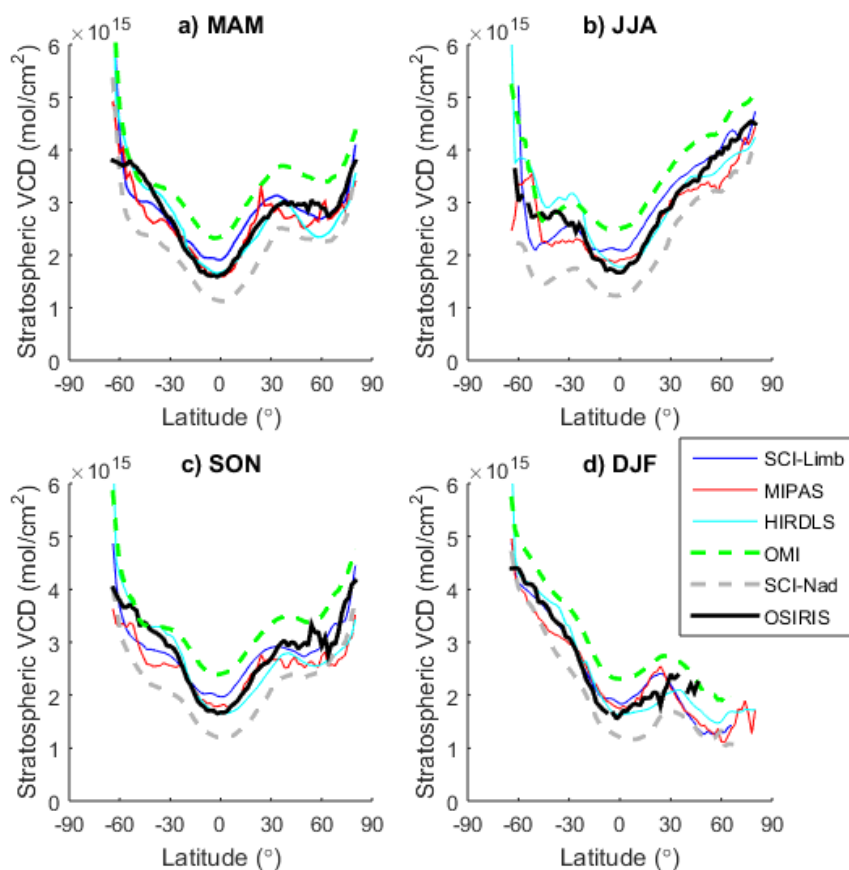
Figure A2: Seasonal averages of stratospheric NO₂ VCDs for 2005-2007 in 2° latitude bins

for (a) March-April-May (MAM), (b) June-July-August (JJA), (c) September-October-

November (SON) and (d) December-January-February (DJF). SCIAMACHY limb (blue

line), MIPAS (red line), HIRDLS (cyan line), OMI (green dashed line), SCIAMACY nadir

(grey dashed line), and OSIRIS (thick black line) are all shown. Figure is adapted from

Belmonte Rivas et al. (2014).